Preliminary Deposition Modeling: For Determining the Deposition of Corrosive Contaminants on SNF Canisters

Spent Fuel and Waste Disposition

Prepared for
US Department of Energy
Spent Fuel and Waste Science and Technology
Philip Jensen, Sarah Suffield, Christopher Grant, Casey Spitz, and Joshua Simmons
Pacific Northwest National Laboratory

January 24, 2020
M3SF-20PN010207045
PNNL- 29620

SUMMARY

This report fulfills the M3 milestone M3SF-20PN010207045. During fiscal year (FY) 2019, Pacific Northwest National Laboratory (PNNL) worked to develop initial deposition and particle tracking models which could be used to better understand how corrosive contaminants deposit on the surfaces of spent nuclear fuel (SNF) canisters during dry storage. These models may be useful in understanding the likelihood of chloride induced stress corrosion cracking (CISCC) on SNF canisters.

Three systems were modeled in FY19. The first was the Sandia National Laboratories (SNL) Dry Cask Simulator (DCS). The SNL DCS is a scaled representation of a canister in a dry cask storage system. It is designed to test key features of canister performance and served as a good testbed for the modeling methodologies that were developed as a part of this effort. The second model is a realistic model of the MAGNASTOR® system, a vertical SNF canister system. The third model is a realistic model of the NUHOMS®, a horizontal SNF canister system.

The particle tracking models and deposition results for each of the three systems are reported herein. These include models with varying decay heat rates, varying particles size distributions, driving winds, etc. The model results are further broken down and show the deposition on specific areas of the canisters (i.e., top, walls, etc.). This is important because different areas of the canisters are more susceptible to CISCC.

All models presented herein predict a low level of deposition on the canisters. For the two models based on actual canister systems (MAGNASTOR® and NUHOMS®), very little (in some case less than 1%) deposition was predicted at the canister walls which is the area most susceptible to CISCC. However, it is important to note, that these results should not be taken at this time to imply that the total mass loading on the canisters is low. To determine the total mass loading on a canister, one would need to know the actual contaminant load in the air. Currently, there is very little information available concerning the atmospheric contaminant concentration at Independent Spent Fuel Storage Installation (ISFSI) sites. The lack of ISFSI contaminant information also drove the decision to use a uniform particle size distribution as an input to these models. The uniform particle size distribution is hypothetical, and it is important to note that the deposition results are a function of this hypothetical input. In the future, when actual ISFSI site contaminant data is available, these models could be easily adapted to use these actual data sets. The models presented herein are a useful capability for analyzing canister performance and a good first step in understanding the deposition of corrosive contaminants on canister surfaces, but many information gaps remain.

Please Note: When interpreting this report, the results should be taken as information only. The methods used to model deposition are preliminary and have not been verified and validated. Future modeling and testing are planned. Future modeling will be needed to refine the models and methods used herein. Future testing will be needed to verify and validate the models. Verification and Validation of these models will be needed, if models such as these are to be used to predict the likelihood to CISCC on SNF canisters.

This page is intentionally left blank.

ACKNOWLEDGEMENTS

The authors would like to thank our U.S. Department of Energy sponsor, Ned Larson, for funding and supporting this work. We would also like to thank our collaborators at Sandia National Laboratories.

This page is intentionally left blank.

CONTENTS

This page is intentionally left blank.

LIST OF FIGURES

LIST OF TABLES

This page is intentionally left blank.

ACRONYMS

BWR	boiling water reactor
CAD	computer-aided design
CDF	cumulative distribution function
CFD	Computational Fluid Dynamics
CISCC	chloride induced stress corrosion cracking
DCS	Dry Cask Simulator
DOE	U.S. Department of Energy
DSC	Dry Shielded Canister
EPRI	Electric Power Research Institute
FY	fiscal year
ISFSI	Independent Spent Fuel Storage Installation
NRC	U.S. Nuclear Regulatory Commission
PNNL	Pacific Northwest National Laboratory
SNF	spent nuclear fuel
SNL	Sandia National Laboratories
SSA	sea-salt aerosol

This page is intentionally left blank.

PRELIMINARY DEPOSITION MODELING: FOR DETERMINING THE DEPOSITION OF CORROSIVE CONTAMINANTS ON SNF CANISTERS

1. INTRODUCTION

This report describes preliminary particle tracking and deposition models, which were developed to predict the deposition of corrosive contaminants on spent nuclear fuel (SNF) canisters. These models may be useful for determining the likelihood of chloride induced stress corrosion cracking (CISCC) on SNF canisters. In the area of canister CISCC, significant previous work has been done by Sandia National Laboratories (SNL), the Electric Power Research Institute (EPRI), Pacific Northwest National Laboratory (PNNL), etc. However, no prior work has been done to examine the deposition of corrosive contaminants on SNF canister surfaces. The models presented herein are an important first step in understanding how corrosive contaminants deposit on actual canister surfaces, and the rate at which they deposit. Models such as these may be key because if they are verified and validated, they could be extended to encompass all canister designs and it would allow for the prediction of canister contaminant deposition at any Independent Spent Fuel Storage Installation (ISFSI).

Three separate deposition and particle tracking models were developed for this effort.

1) SNL Dry Cask Simulator (DCS) Canister: The SNL DCS is a scaled test facility of a canister system. The SNL DCS was included in our deposition modeling efforts because it was a good testbed for the modeling methodologies developed herein. The DCS modeling results shown in this report also include several results which are not included for the other two cases. These results include wind effects and detailed deposition for a given particle size. In the future, similar modeling is planned for the MAGNASTOR® and NUHOMS® models.
2) MAGNASTOR®: The MAGNASTOR® system is vertical SNF canister system designed and built by NAC International. Realistic particle tracking and deposition modeling, for various decay heat rates are reported.
3) NUHOMS®: The NUHOMS® system is a horizontal SNF canister system designed and built by TN Americas. A site-specific variant of the standard NUHOMS® at Calvert Cliffs Nuclear Power Station's ISFSI was modeled. Realistic particle tracking and deposition modeling, for various decay heat rates are reported.

1.1 Model Limitations and Disclaimer

The modeling results shown herein are preliminary and for information only. The models are useful for understanding the physics of particle tracking and deposition, as it applies to SNF canisters. However, they are not the final analysis of the systems discussed herein, and additional model development and testing will be needed before models such as these can be credited for determining the likelihood CISCC on SNF canisters.

While the PNNL thermal models are well developed, the deposition models are preliminary and will require further development.

The deposition models, deposition results, and the deposition modeling methodology described in this report are not verified and validated. Detailed and thorough testing is required to verify and validate these models. Such testing is required before deposition modeling such as this can be used to predict actual deposition on deployed canister at ISFSI sites.

This page is intentionally left blank.

2. BACKGROUND

2.1 SNF Canister CISCC Background and Discussion

Nuclear power plants produce SNF, which is considered radioactive waste under current U.S. policy. It is possible that SNF will be stored at the reactor site or consolidated interim storage facilities for periods longer than a century. The U.S. Nuclear Regulatory Commission (NRC) has concluded that SNF generated by any reactor can be safely stored for 60 years beyond the licensed life of a reactor. Furthermore, it has been acknowledged that for "long-term storage" of up to 160 years beyond the licensed life of the reactor "one time replacement of the ISFSIs and spent fuel canisters and cask" may be required (NRC 2014). At present, the technical basis is insufficient to support long-term storage without the replacement of the spent fuel canisters. In addition, without future policy action, one must assume and plan for extended SNF storage at ISFSI locations.

During dry storage the primary degradation process is likely to be CISCC at the heat affected zones of the canister welds (NRC 2012). While it is currently unknown if there is a threshold concentration for CISCC initiation; it can be assumed that the onset and progress of material degradation will depend on local contaminant concentration, the properties of the contaminant species, and synergistic effects when multiple contaminants are present. The primary contaminant of concern is chloride, which is dispersed in the atmosphere and then deposits on to the canisters. Currently, the rate of chloride deposition onto the canisters is unknown. This study is a necessary first step, which will allow for a better understanding of the deposition rate and the location of deposition on canister components.

2.2 Deposition Mechanisms

In the air, there are suspended solid particles and liquid droplets known as aerosols that can be transported over vast distances and for long time periods. However, the number of particles in the air is constantly changing through various mechanisms. During deposition, particles leave the air and attach to a surface. Resuspension and generation cause particles to enter the air, either by detaching from a surface or by producing from a source. For the nuclear industry, a major concern is the deposition of sea-salt aerosols (SSAs) onto the surface of dry storage canisters at ISFSIs. SSAs are generally generated through the volatility of ocean water. These SSAs can then be carried in the air to inland ISFSIs (EPRI 2015, Jensen et al. 2016). Currently, the deposition of these SSAs onto dry storage canisters is studied as a source for potentially initiating CISCC. In order to better understand the potential for the deposition of SSAs onto the surfaces of dry storage canisters, it is necessary to adequately model the mechanisms responsible for deposition within dry storage systems at ISFSIs.

The following discussion introduces mechanisms involved in aerosol transport and deposition that are not necessarily standard inclusions in deposition models and evaluates their importance in modelling, specifically concerning dry storage at ISFSIs. The models developed in FY19 incorporate some of the effects listed below, but at this time they are not all inclusive. Additional modeling is needed to incorporate more deposition mechanism, and analytical studies need to be performed to determine the importance of each mechanism.

- Brownian Diffusion: Brownian diffusion involves the seemingly random motion of aerosols within a carrier fluid. When impacts from the carrier fluid are greater on one side of an aerosol than the other, the aerosol changes direction. When the Brownian motion of an aerosol causes it to deposit onto a surface, it is referred to as Brownian deposition. Brownian deposition can be responsible for small aerosols being able to cross the laminar boundary layer of smooth surfaces in order to deposit. Brownian motion is typically considered for aerosols with submicron diameters (Camuffo 2014; Li 1992; Tang 2012; Sugiyama 2014). SSAs are expected to be larger than what would be expected to experience Brownian deposition, so Brownian deposition may not be a crucial factor to consider for dry storage systems.

- Aerodynamic Deposition: There are two means of aerodynamic deposition; impaction and interception. Both of these means involve an aerosol following a bulk flow. When the flow changes direction, aerosols will experience a drag force that isn't in the same direction as their momentum. This drag force may or may not be able to overcome the aerosol's momentum for the aerosol to change directions with the bulk flow (Sugiyama 2014; Camuffo 2014). When momentum is the prevailing factor, the aerosol could experience impaction. In impaction, the aerosol may maintain its trajectory and potentially deposit on the surface that caused the change in direction of the bulk flow. When the drag force and momentum are balanced, the aerosol could experience interception. In interception, the aerosol may change directions with bulk flow but still move close enough to and potentially deposit on a surface. Aerodynamic deposition will be expected in any deposition models for dry storage at ISFSIs. The prevalence of this mode of deposition will be dependent on flow paths and bulk flow velocity within individual storage configurations.

- Gravitational Settling: When aerosols are suspended in air, they are kept aloft by viscous drag and buoyancy effects. However, aerosols also experience gravity. In still air and for large aerosols especially, gravity will cause aerosols to settle to the bottom of the air volume and deposit. SSAs are expected to be large enough to be influenced by gravitational settling, so this mechanism should be included in ISFSI deposition models. Gravitational settling is expected to be especially important in horizontal storage systems where the horizontal surface area is much greater, and in storage systems where the spent fuel has cooled to a point where natural convection in the system is reduced.

- Thermophoresis: Thermophoresis describes motion of an aerosol in the opposite direction of a temperature gradient (Talbot, et al. 1980). The general concept behind the mechanism is that in a gas between two surfaces of differing temperatures, the gas particles near the warmer surface will have more momentum than those near the cooler surface. The result is a greater force being exerted on an aerosol by the gas particles with greater momentum, causing the particle to move away from the warm surface. However, many factors are involved in determining the impact of thermophoresis, including both the aerosol's and the gas' properties. For modelling aerosol deposition at ISFSIs, thermophoresis should be considered as potentially significant due to the heat generation of spent fuel. For long-term storage in dry storage casks at ISFSIs, thermophoresis may become less important depending on the level of heat generation from the spent fuel, which will be especially important to understand since thermophoresis is expected to potentially inhibit aerosols from depositing on dry storage canister surfaces.

- Turbophoresis: Turbophoresis is the motion of an aerosol that is caused by differing levels or turbulence. Again, due to the momentum of surrounding gas particles, an aerosol tends to move from regions of higher turbulence towards regions of lower turbulence (Reeks 1983; Young 1997). In channel flow, the impact of turbophoresis is for aerosols to move towards the walls of the channel. Considering dry storage systems, the channels used for airflow could result in aerosols moving closer to the cask wall, meaning turbophoresis could potentially promote aerosol deposition.

- Saffman Lift: Saffman lift is the motion of an aerosol caused by shear on the surface of the aerosol. This shear can be caused by the aerosol rotating relative to the bulk flow or by a velocity gradient in the bulk flow perpendicular to the direction of flow. Depending on the relative velocities of the aerosol and the bulk flow, Saffman lift can result in movement either towards or away from a channel wall (Saffman 1965; Lau 2014). Saffman lift is usually considered for submicron particles and will likely be negligible when considering SSAs at ISFSIs.

- Diffusiophoresis: Diffusiophoresis is the motion of aerosols caused by a gradient in the concentration of gas particles. Since a fluid will naturally try to reach equilibrium, gas particles

will diffuse between two different species of gases. If this diffusion is great enough, any suspended aerosols will experience forces from these moving gas particles. Depending on the rate of diffusion and the particles involved, one species could impart more force onto an aerosol, resulting in a net force in one direction (Housiadas 2012; Sugiyama 2014). In dry storage systems at ISFSIs, diffusiophoresis would potentially be important during conditions in which condensation or evaporation of water vapor occurs. In the case of evaporation of water from a surface, the high concentration of water vapor molecules would diffuse away from the surface, while air molecules would diffuse towards the surface. Aerosols would be expected to be pushed towards the surface due to the heavier mass of air molecules compared to water molecules. In the case of condensation of water onto a surface, aerosols would be expected to be pushed away from the surface because of the low concentration of water vapor molecules near the surface. However, these same conditions could also cause Stefan flow to occur, which might counteract the effect of diffusiophoresis.

- Stefan Flow: Stefan flow is experienced during condensation or evaporation of a gaseous material. In the case of condensation, Stefan flow causes aerosols to be pushed towards a surface. In the case of evaporation, aerosols are pushed away from the surface (Housiadas 2012). Since this mechanism can act in opposition to thermophoresis and diffusiophoresis, it may be considered important in ISFSI deposition modelling. Both diffusiophoresis and Stefan flow should be considered for ISFSI deposition modelling, but further analysis into particle distributions, as well as condensation and evaporation expectations within a dry storage system, could determine that these two mechanisms are less prevalent than others.
- Electrophoresis: Electrophoresis is the motion of aerosols caused by electrostatic forces. In the presence of an electric field, charged aerosols will be influenced, resulting in motion. With many charged aerosols in air, the motion may be caused by the electric fields of other surrounding charged particles. In general, electrophoresis is important at low relative humidity since electric charge cannot dissipate as easily in low relative humidity (Camuffo 2014). Because of this fact, site location could be used to help inform the decision to include electrophoresis in ISFSI deposition modelling.

This page is intentionally left blank.

3. DEPOSITION MODELS

All the models presented in this report were previously developed as thermal models to predict component temperatures within the storage cask. PNNL has extensive experience developing thermal models for storage and transportation canisters of SNF. The PNNL thermal models are well suited for looking at particle deposition, since the flow and temperature profiles have already been setup and solved. Particle deposition is incorporated by adding particle tracking sub-models to the physics of the thermal model, creating particle injectors at the inlets and iterating the solution with particle tracking on.

A steady state model of various canister storage systems was set up with STAR-CCM+ (Siemens PML Software, 2019). STAR-CCM+ is a commercial computational fluid dynamics (CFD) software package. The segregated flow solver with a K-Omega turbulence model was applied to the model. Air cools the canister through natural convection driven flow. The air is modeled as an ideal gas with constant density and gravity turned on to account for buoyancy effects. A Lagrangian multiphase model was set up to track particles traveling through the canister storage system. The particles were assumed to be spherical in shape and assumed to have the density of sea water. This is because the most likely chloride source is SSAs. This assumption is only partially justified, because SSAs are known to change in density as they travel through the atmosphere by responding to changes in relative humidity (i.e., absorb or shed water as relative humidity changes) (Gong et al. 1997, Tang et al. 1997, Lewis & Schwartz 2004). As such, this assumption is likely most valid for sites near to the source of SSA generation (i.e., coastal locations) because the distance traveled between the point of generation and receptor is minimal, with very little change in relative humidity. Future modeling and testing are planned and will examine the effects of particle density, and sensitivity studies will be performed to determine how density affects deposition. Also, future work is needed to characterize the particle size distribution and particle morphology at ISFSI sites. A stuck boundary condition was applied along all surfaces in contact with air. The stuck boundary condition assumes that if a particle reaches a wall boundary, the particle sticks to the wall. At this time, resuspension of particles is not included in the models.

The deposition models also include user defined drag function and thermophoretic force (Greenfield et al. 1998, Sagot et al. 2009, Talbot et al. 1980, Siemens PLM Software 2019). Future modeling work will further refine the deposition modeling, refine the user defined functions, and include additional effects, such as additional phoretic mechanisms and a multi-phase model to show the effects of humidity.

Currently, all models use a uniform particle size distribution ranging from 0.25-25 μm, as the input. The range of 0.25-25 μm was chosen because it represents the minimum and maximum bounds that were most commonly found in literature for SSAs (Lewis & Schwartz 2004). However, the upper and lower limits of the particle size distribution can vary greatly depending on the local conditions. Because of this, future modeling work and testing is necessary to examine how the particle size distribution and the upper and lower bounds affects deposition. A uniform distribution was chosen, because no particle size distribution data exists for an ISFSI site. Some data sets exist which examine the particle size distribution and SSA size distribution at various sites across the USA (Zhao et al. 2008, Jordan et al. 2015, Taiwo et al. 2014, Milford et al. 1985, Xia et al. 2010), however it is difficult to assess the applicability of these data sets for ISFSI sites because ISFSIs are located at numerous locations with very different climatic conditions. For model testing purposes, an actual particle size distribution was tested with some of the models presented herein and no problems with inputting this data set into the models was seen. However, this data is not reported because it is not representative of an actual ISFSI site. The lack of particle size distribution data for ISFSI sites is a critical issue and knowledge gap. Obtaining particle size distribution data will be key, if models such as these were to be extended to actual SNF canisters at ISFSI sites.

3.1 Dry Cask Simulator Model

A CFD model of the SNL DCS was constructed using the commercial software STAR-CCM+ (Siemens PLM Software, 2019). The CFD modeled the parts that make up the fuel region assembly as a single porous regions.

The purpose of the DCS was to produce validation-quality data that can be used to test the validity of thermal qualification models used to determine peak cladding temperatures in vertical dry storage casks. The DCS is constructed of an electrically heated but otherwise prototypic boiling water reactor (BWR) Incoloy-clad test assembly inside a storage basket and cylindrical pressure vessel that represents a vertical canister system. The canister is surrounded in a carbon steel shell to represent a convection cooled aboveground dry cask system. The pressure vessel canister was filled with helium gas and pressurized. Air enters the system through the inlets near the base and exits though the outlets located near the top. The geometry and material property details of the DCS are described in the DCS handbook (Durbin & Lindgren 2017).

The geometry for the CFD model was generated using the commercial computer-aided design (CAD) software SolidWorks (Dassault Systemes SolidWorks Corp. 2017). The CAD geometry was constructed from drawings and details listed in the DCS handbook (Lindgren and Durbin 2017).
The CAD geometry is shown in Figure 1, Figure 2, and Figure 3.

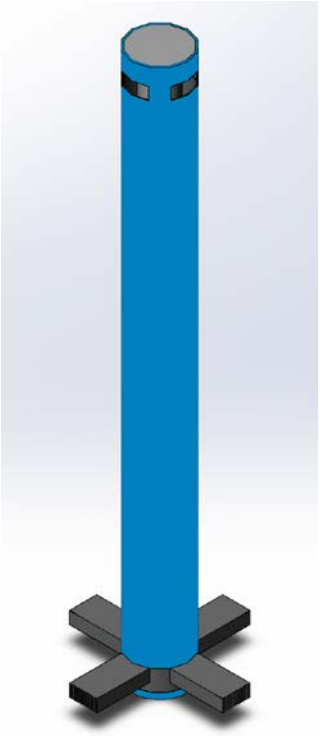

Figure 1: CAD geometry of DCS – exterior view.

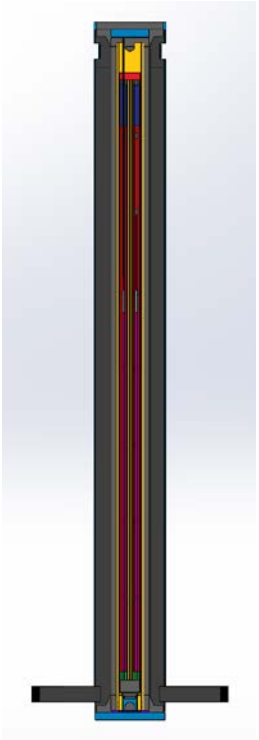

Figure 2: CAD geometry of DCS – axial cross-sectional view.

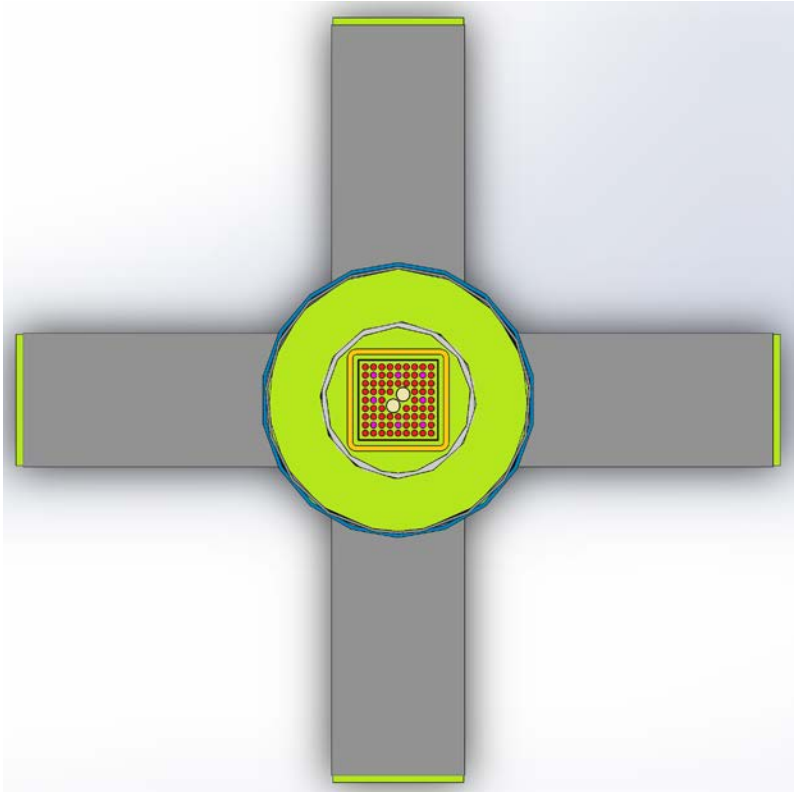

Figure 3: CAD geometry of DCS – radial cross-sectional view at 75 inches from the top of the bottom plate.

The SolidWorks geometry was imported into STAR-CCM+. The geometry was then meshed into regions connected by interface boundaries, resulting in a single conformal polyhedral volume mesh across all regions. Along each wall/fluid interface, the mesh contains a prism cell layer to improve the accuracy of the flow solution near the walls. The prism cell layer consists of orthogonal prismatic cells adjacent to the wall boundaries. The prism cell layer in the air region was four cells thick and two cells thick in the helium region. For computational efficiency, a quarter section model of the geometry was meshed, and symmetry boundaries were applied to the model. A radial cross-section of the quarter model mesh through the center of the DCS is shown in Figure 4. Also, for computation efficiency the BWR fuel assembly was modeled as porous media regions with calculated effective properties. A detailed description of the DCS porous media model can be found in Suffield et al. 2019.

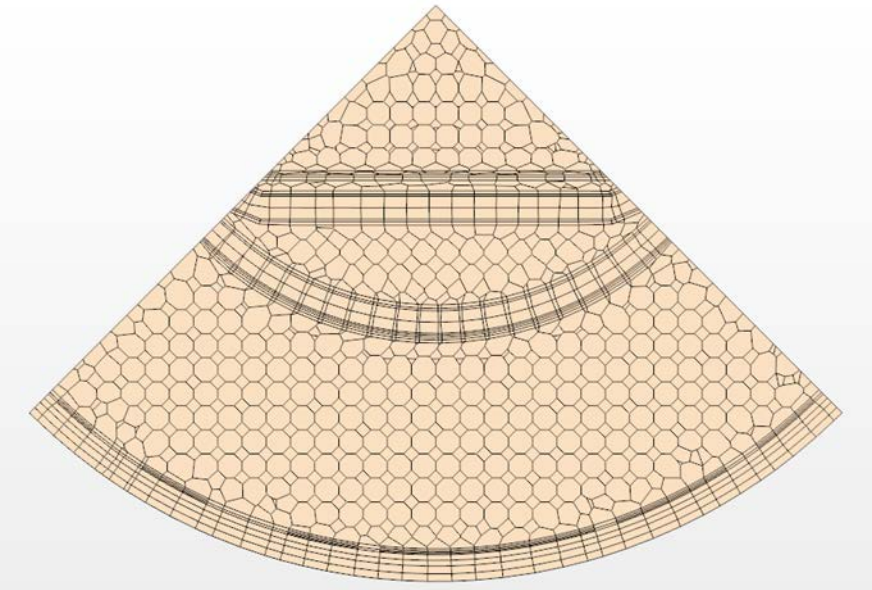

Figure 4: Mesh for quarter model – radial cross-sectional view through center of DCS.

3.1.1 Particle Distribution

The DCS model was initially set up to inject a single particle diameter for a given heat load. The simulated heat loads were 0.5 kW, 1 kW, 2.5 kW, and 5 kW. The ambient environment temperature was set to 27°C. A range of particle diameter cases were run from 0.2–150 um. The particles were injected at the inlet of the DCS. The DCS components where deposition was measured are shown in Figure 5. Resulting plots from the four different head loads are shown in Figure 6, Figure 7, Figure 8, and Figure 9. The plots show that most deposition occurs in the inlet ducts and very little is deposited on the canister wall.

The large upper bound of this range was chosen for demonstration purposes, in order to show how immobile larger particles are (depositing at the inlet shortly after being injected into the model). It is important to note that this range is hypothetical and not representative. The range of 0.2–150 um is only used in the models for Figure 6, Figure 7, Figure 8, Figure 9, and Figure 10. All other models use 0.25-25 µm. As discussed previously, 0.25-25 µm is used for all other models presented in this report because it represents the minimum and maximum bounds that were most commonly found in literature for SSAs (Lewis & Schwartz 2004).

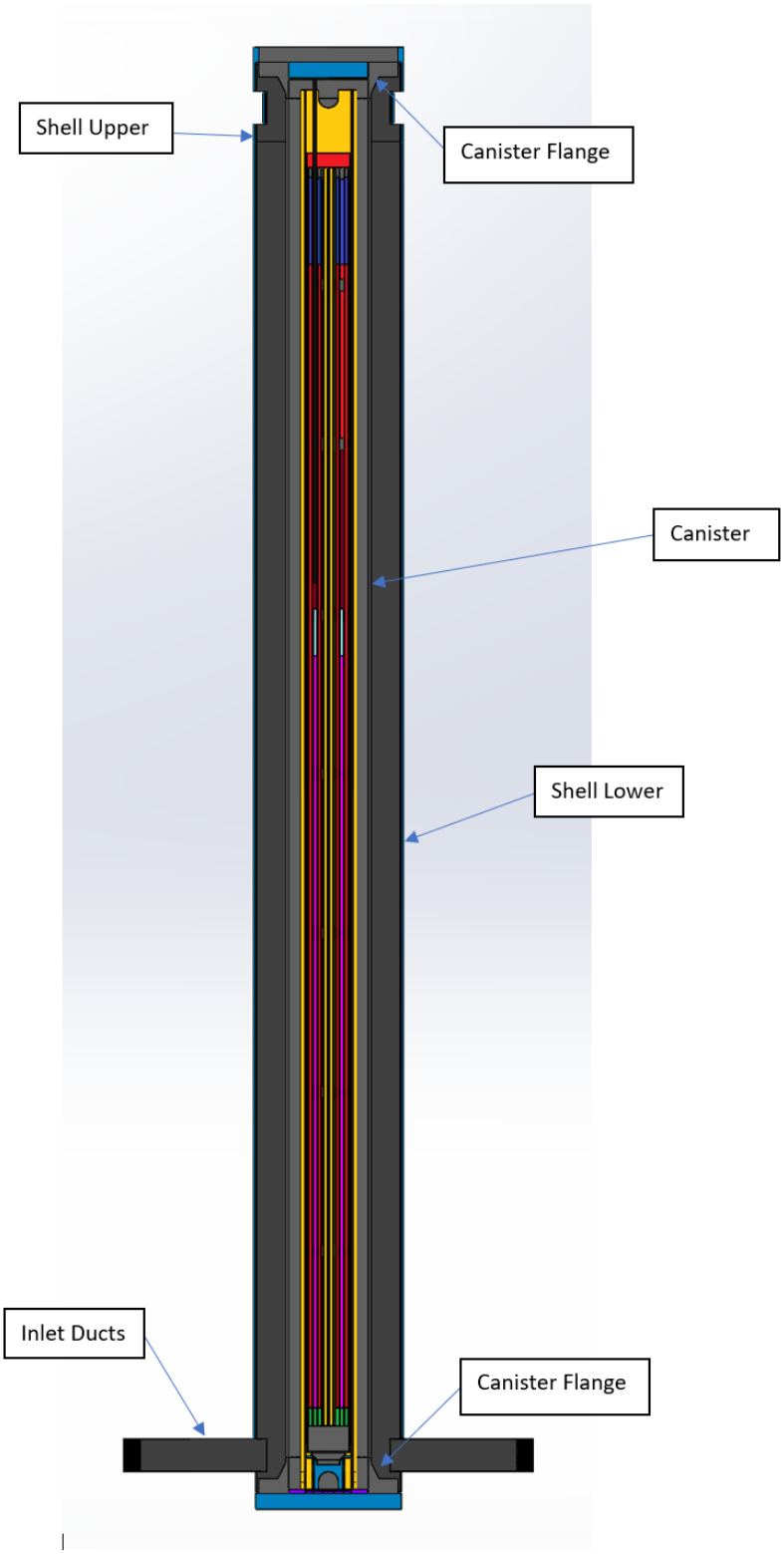

Figure 5: DCS Geometry and components.

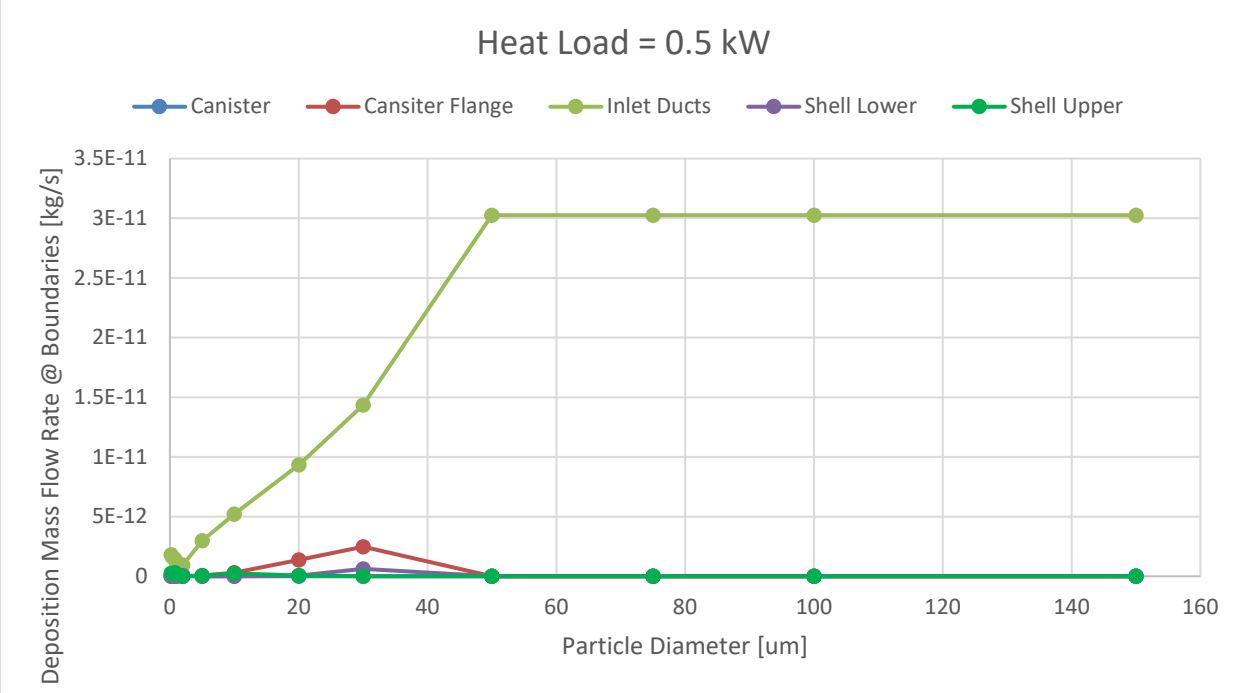

Figure 6: DCS deposition results - heat load = 0.5kW.

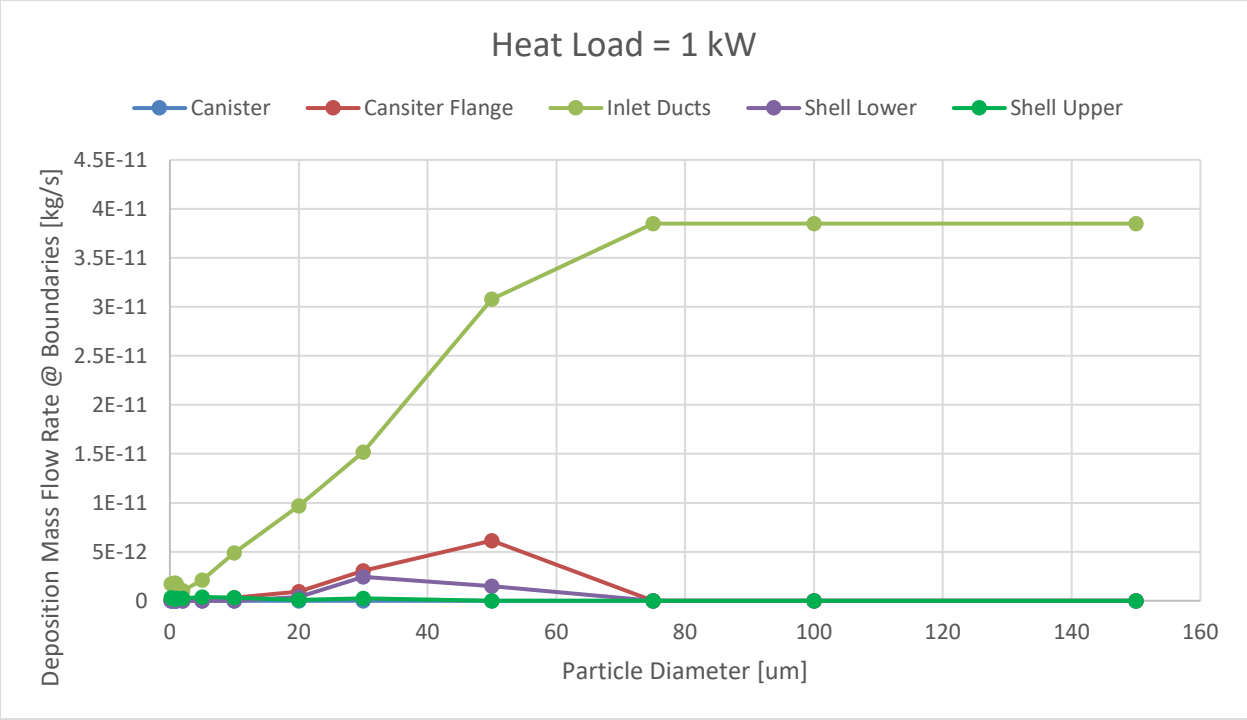

Figure 7: DCS deposition results - heat load = 1kW.

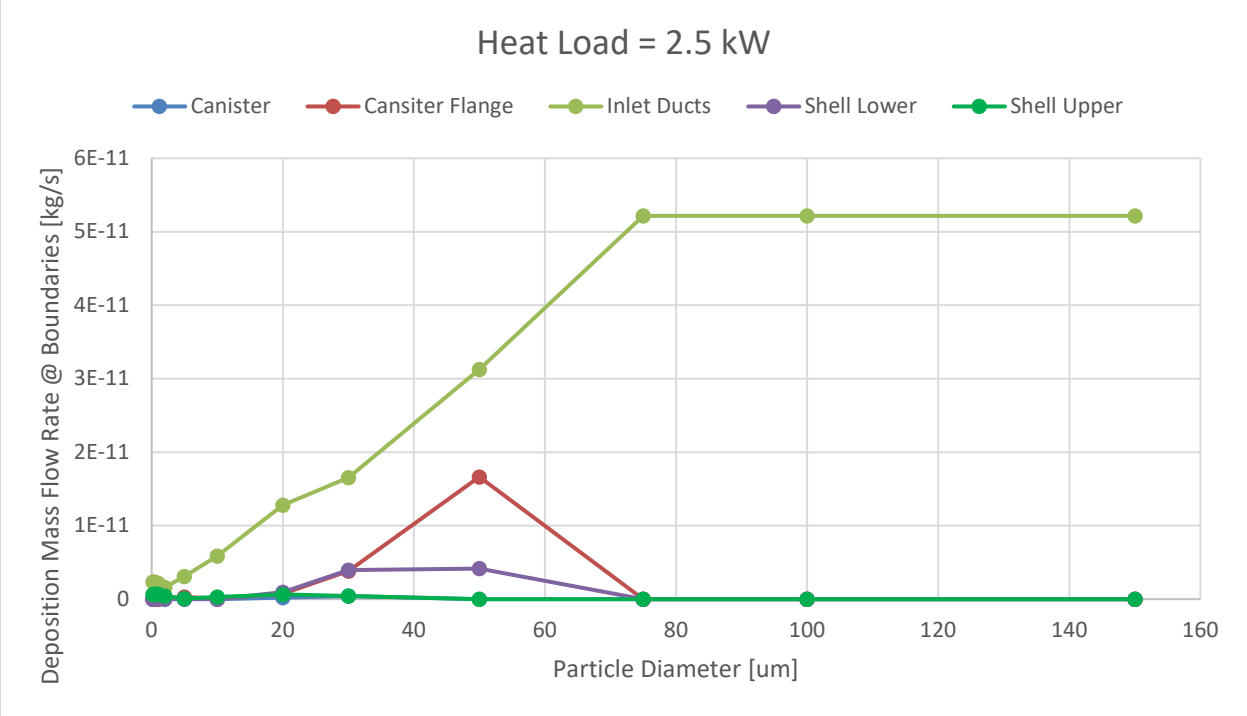

Figure 8: DCS deposition results - heat load = 2.5kW.

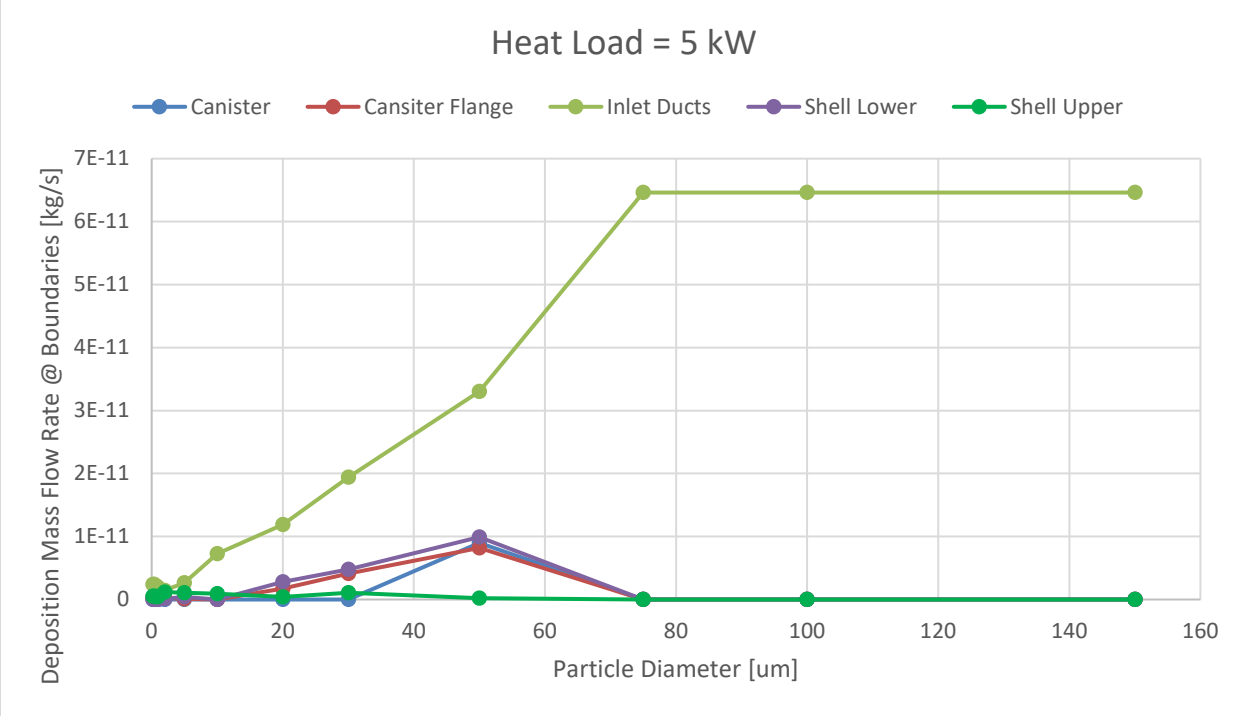

Figure 9: DCS deposition results - heat load = 2.5kW.

A uniform particle distribution ranging from 0.25-25 um was also applied to the DCS model. The uniform distribution was applied to the model by creating a cumulative distribution function (CDF) table for the given range. The resulting overall deposition within the DCS and the particle deposition on the canister surface is shown in Figure 10. Figure 10 shows that the majority of the particles that enter the system exit

without interacting with any surface (approximately 28–35 percent stick inside). Of the particles that stick inside the DCS, only a small percentage adheres to canister walls (less than 5 percent). Most of the deposition occurs in the inlet, as is shown in Figure 11.

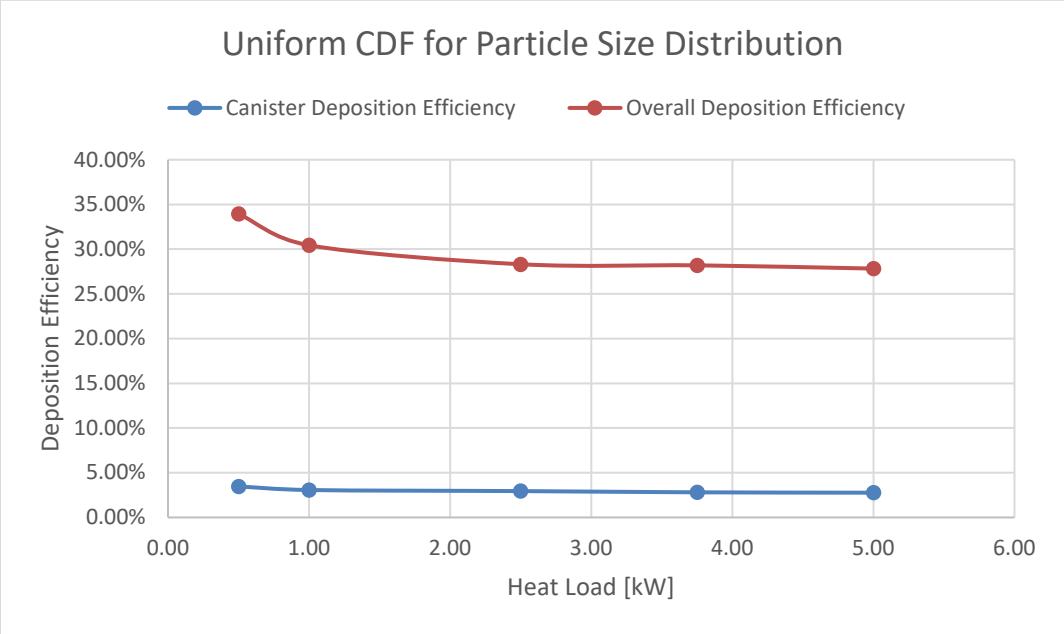

Figure 10: Uniform CDF for Particle Size Distribution

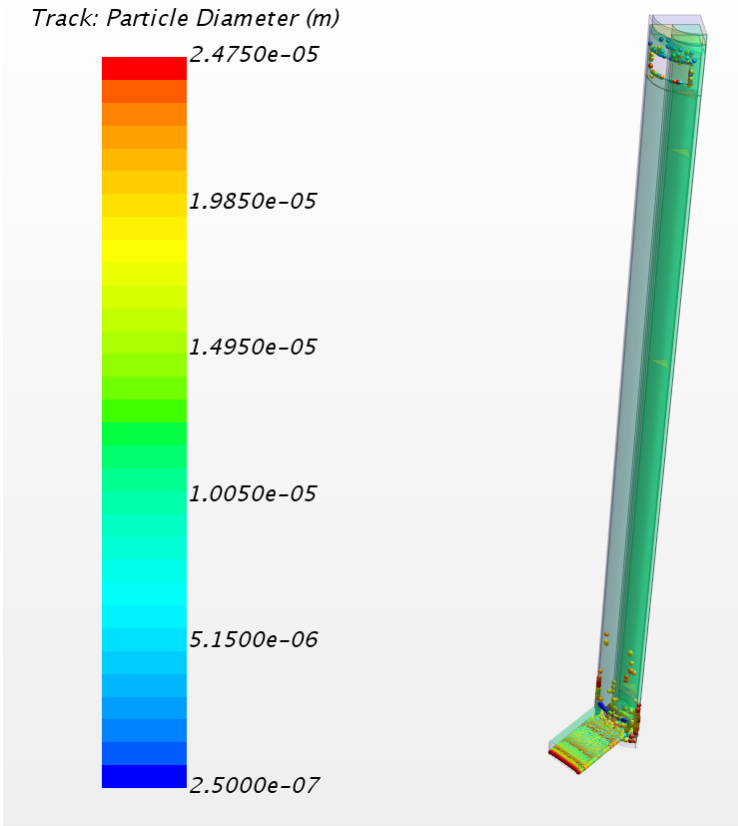

Figure 11: DCS particle deposition with a heat load of 5 kW and a CDF particle distribution

3.1.2 DCS Wind effects Model:

To determine how wind affects the deposition of particles in the DCS, a wind effects model was developed. A control volume was placed around the DCS geometry (to create a wind effects model) to look at how wind external to the DCS would affect flow and particle deposition. The control volume extended approximately 14.5 ft from the DCS inlets on all sides and approximately 18 ft from the top of the DCS. A half symmetry model of the geometry was generated for efficiency. Also, for efficiency the parts internal to the DCS canister were removed and a heat flux boundary condition was applied along the internal surface of the canister. The geometry of the wind effects model is shown in Figure 12. The wind boundary was applied along the X-axis in the positive direction (Figure 13). The wind speed applied at the boundary ranged from 0–40 mph. Three different particle injection configurations were considered; particles injected at the wind boundary, particles injected at the DCS inlets, and particles injected at the DCS inlets and outlets. Results for the three different particle injection configurations are shown in the following section.

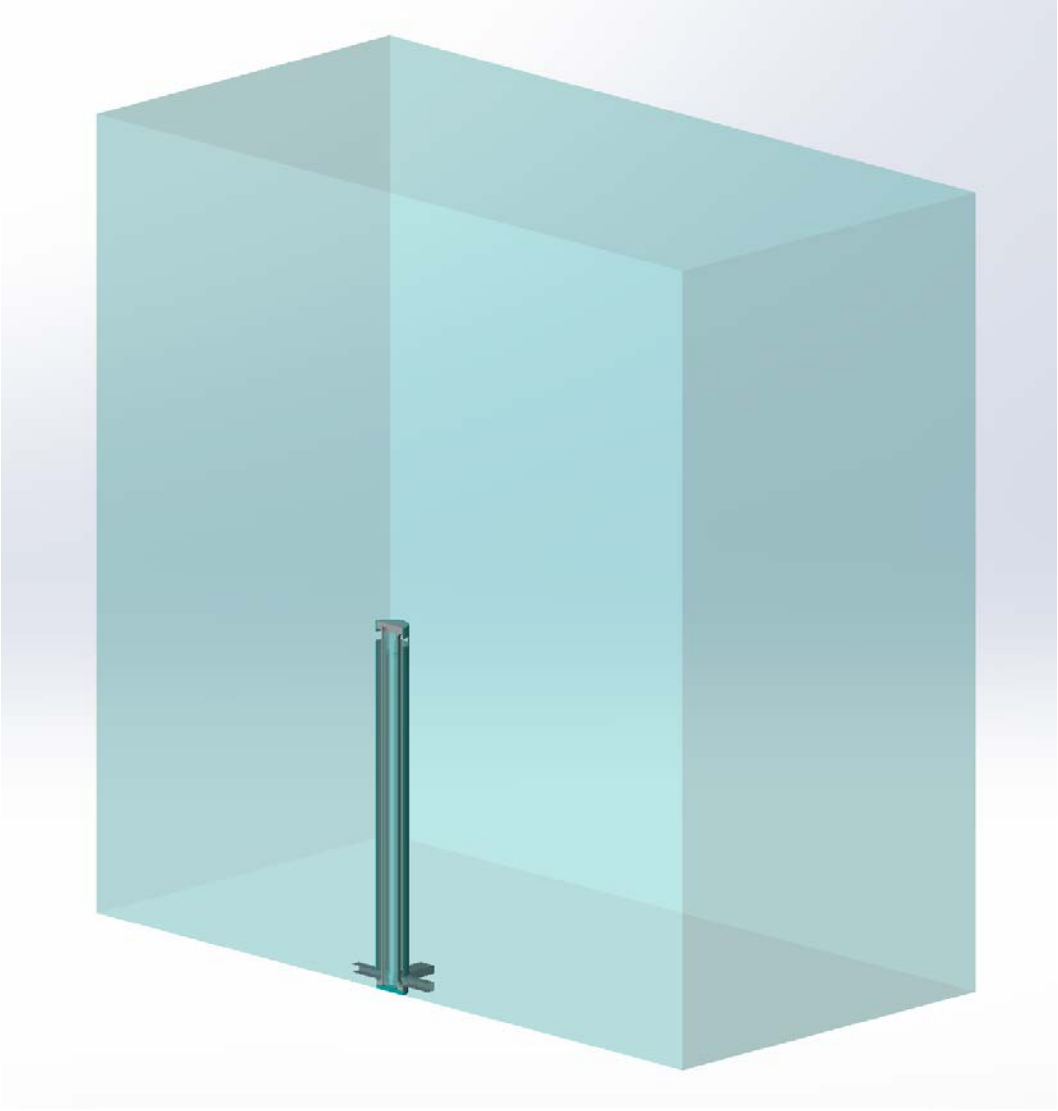

Figure 12: DCS wind effects model – Geometry.

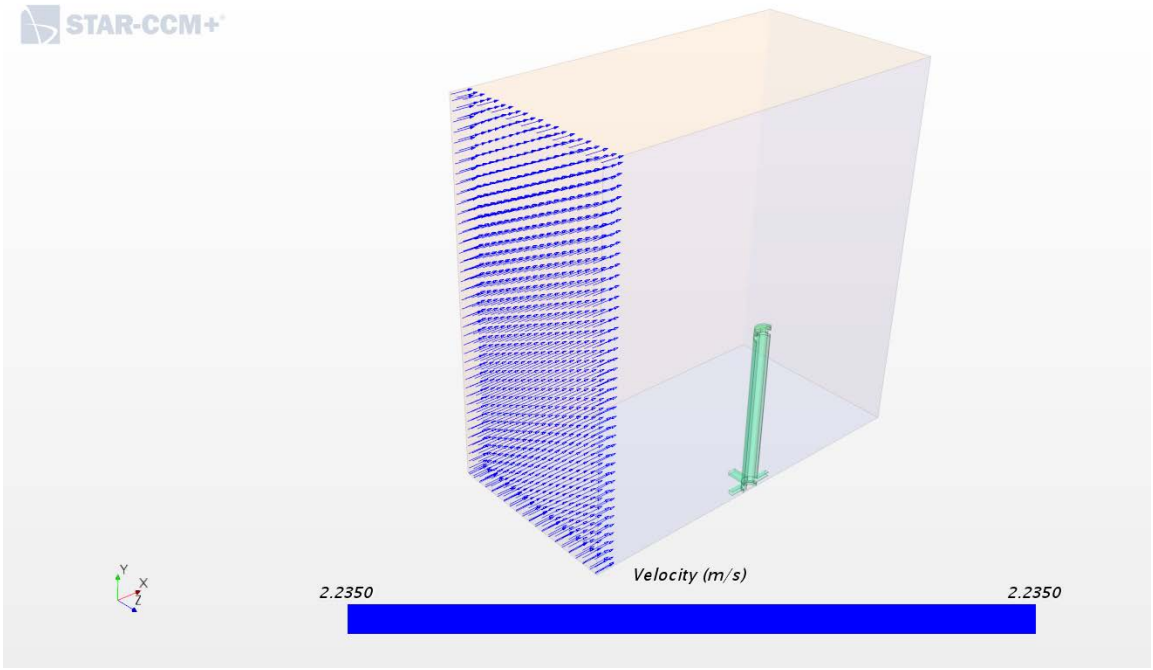

Figure 13: DCS wind effects model – Wind boundary.

3.1.2.1 Boundary Injector

The boundary injector model had the particles injected external to the DCS at the wind boundary. This allowed for a determination of how many particles would end up entering the DCS if the particles were uniformly dispersed in the atmosphere. Figure 14 shows the particle injector location. Result plots are shown in Figure 15, Figure 16, and Figure 17. Figure 15 shows that with a wind speed of 5 mph or greater only 0.1 percent of particles enter the DCS. The greatest number of particles entered the DCS with a wind speed of zero, which represents the natural convection condition. The peak percentage of particles entering the DCS was 0.7 percent for the 5 kW heat load natural convection case. These results indicate that for particles distributed in the surrounding environment, not many would enter the DCS.

For those particles that do make their way into the DCS, Figure 16 shows the percent of particles that would deposit on an inner surface of the DCS. Figure 17 shows that not many of those particles deposit on the heated canister surface within the DCS. The highest particle deposition rates occur for the 5 kW heat load and 40 mph wind case, with 32 percent of particles that enter the DCS depositing and of those particles only a little over 2 percent are deposited on the canister. Figure 18, Figure 19, and Figure 20 show the particle velocity, overall particle deposition, and canister deposition for the 5 kW heat load and 40 mph wind case.

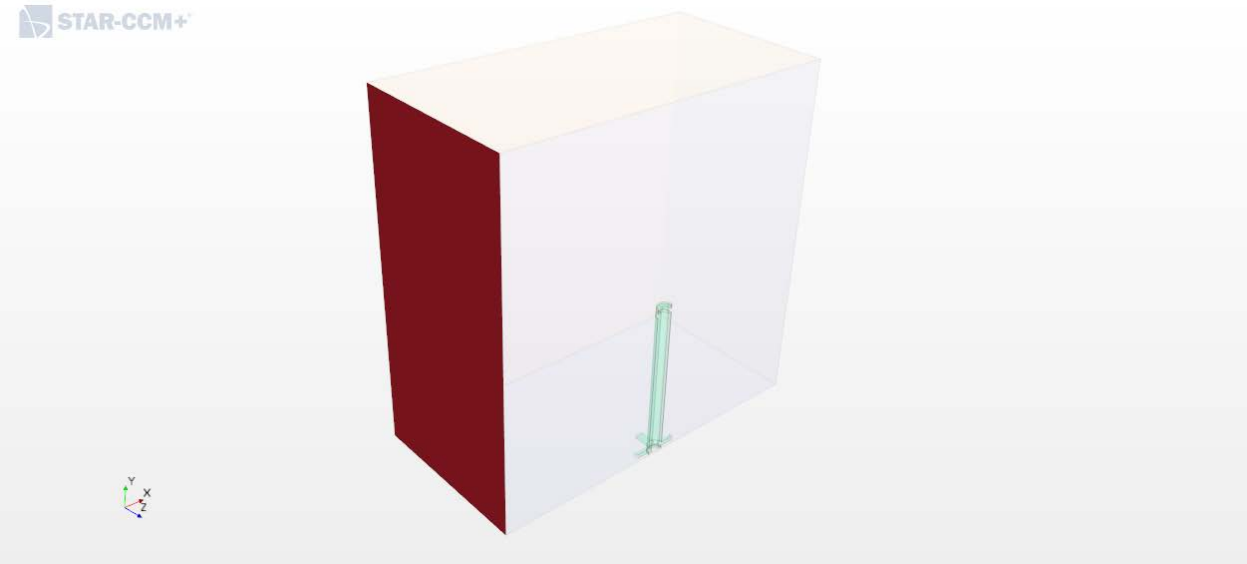

Figure 14: DCS boundary injector wind effects model – Particle injector shown in red.

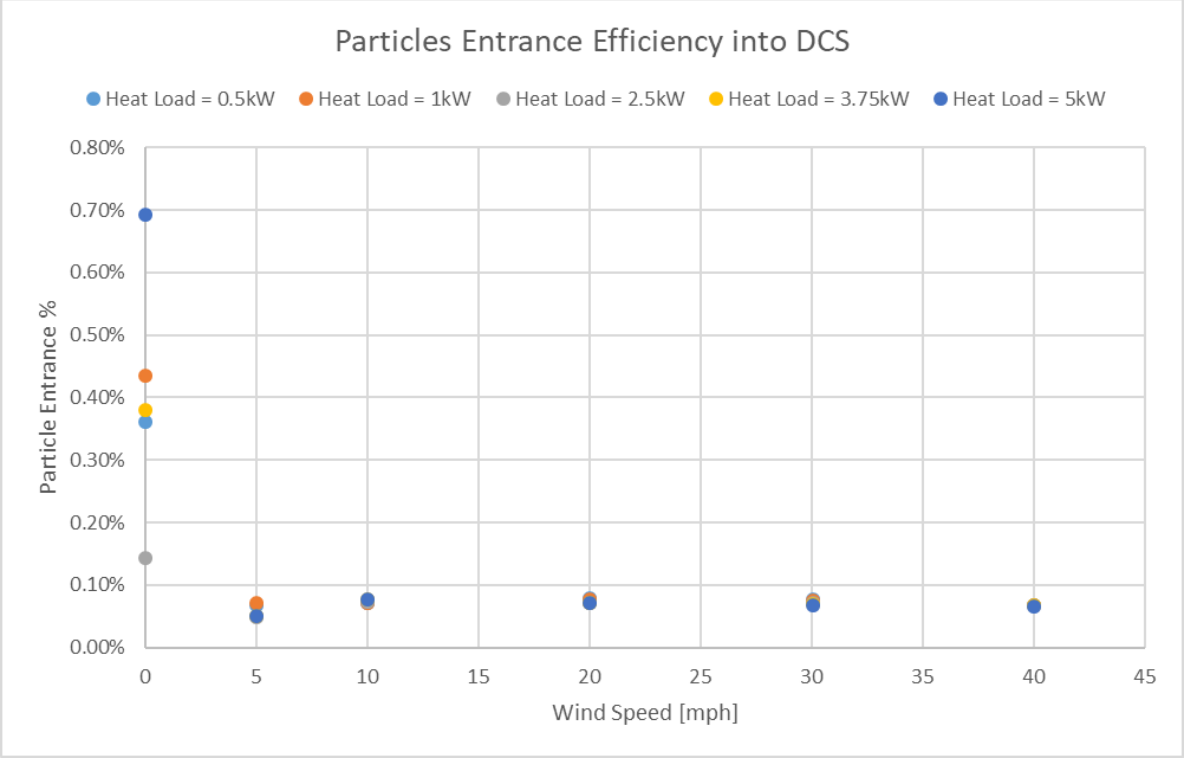

Figure 15: DCS boundary injector wind effects model –Efficiency of particles entering into the DCS.

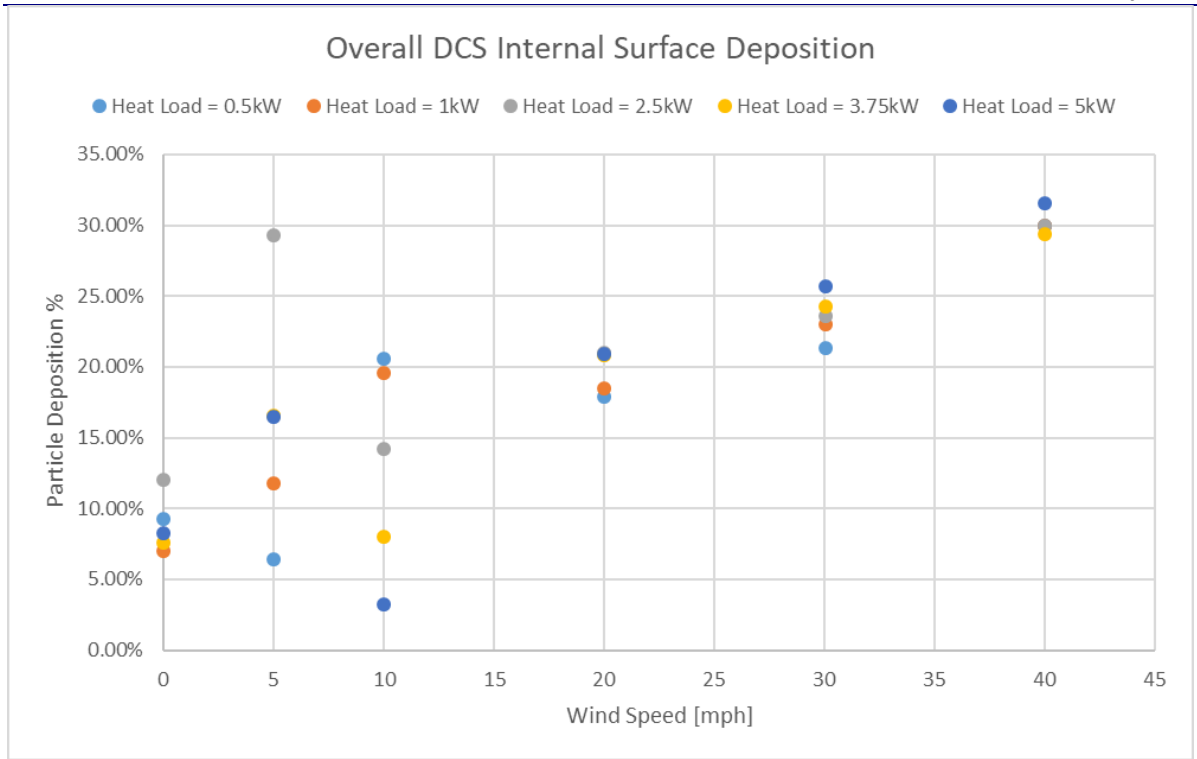

Figure 16: DCS boundary injector wind effects model – Deposition efficiency of particles that have entered the DCS.

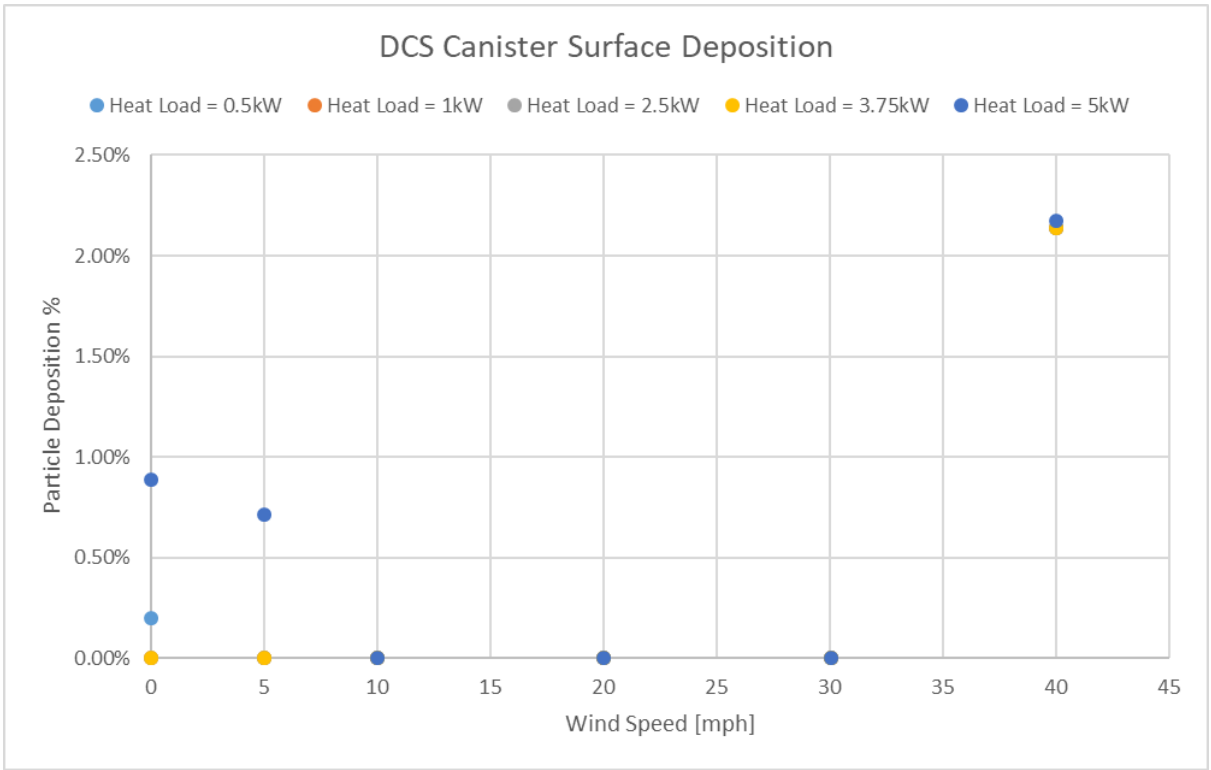

Figure 17: DCS boundary injector wind effects model – Canister deposition efficiency of particles that have entered the DCS.

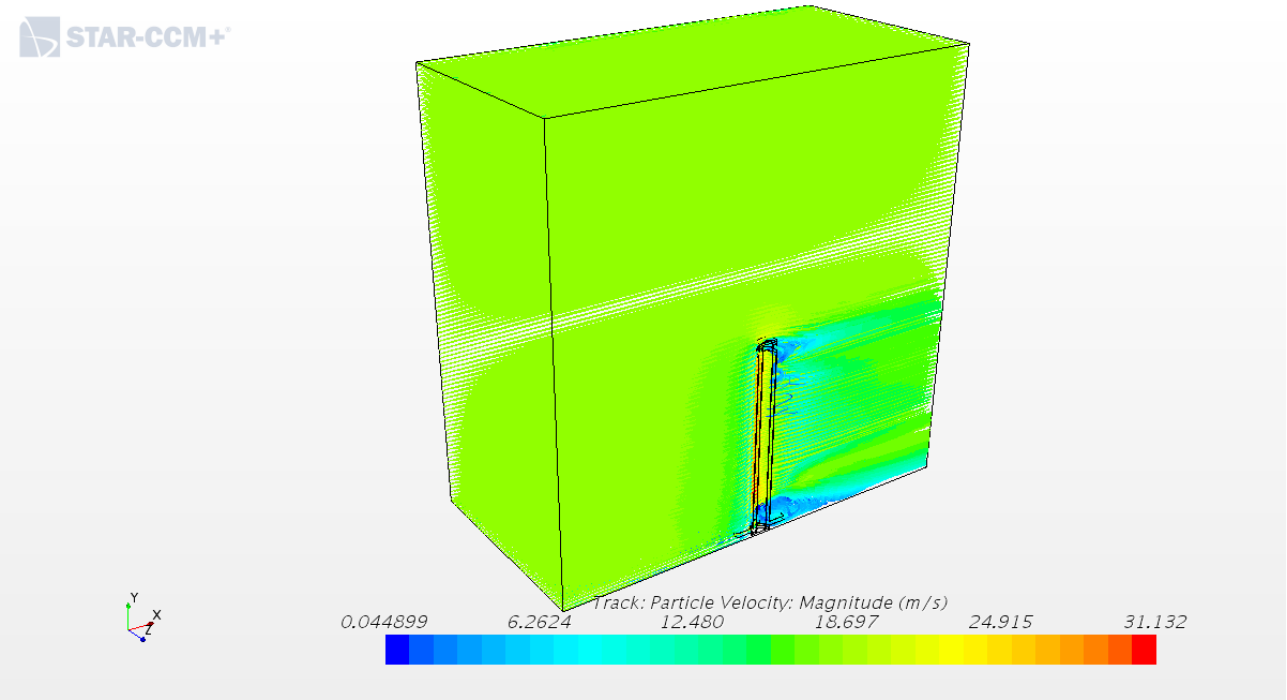

Figure 18: DCS boundary injector wind effects model @ 5 kW and 40 mph wind – Particle velocity.

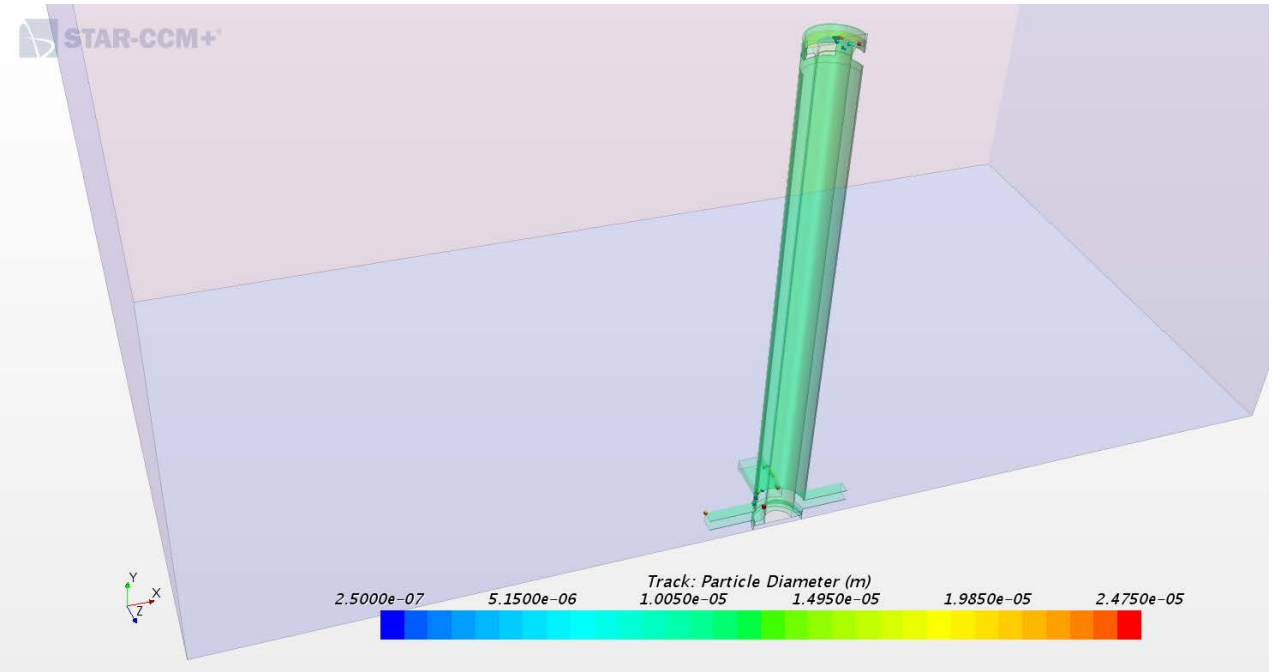

Figure 19: DCS boundary injector wind effects model @ 5 kW and 40 mph Wind – size of particles deposited on DCS surfaces.

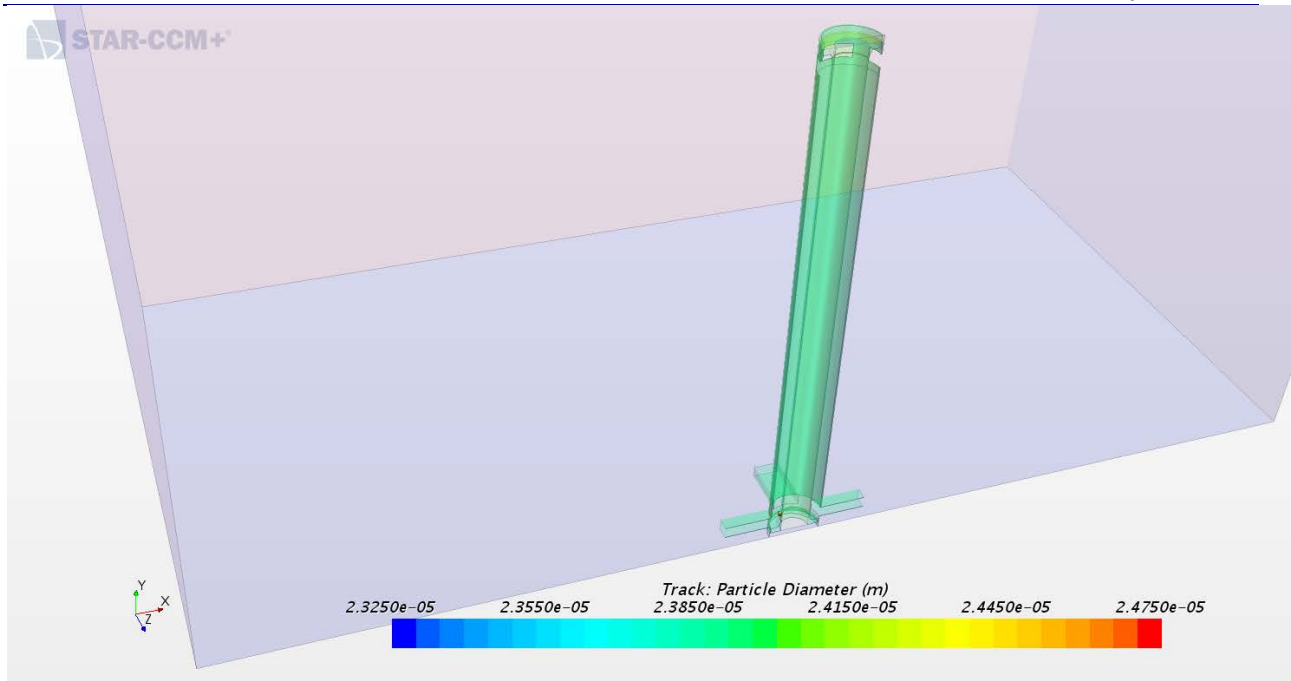

Figure 20: DCS boundary injector wind effects model @ 5 kW and 40 mph Wind – Size of particles deposited on canister surface.

3.1.2.2 Inlet Injector

An alternate configuration was set to inject the particles at the inlets of the DCS. Figure 21 shows the locations of the inlet injectors. The inlet injector model would represent a concentration of particles being displaced right in front of the inlets to the storage cask. The overall particle deposition is plotted for various heat load and wind speed combinations in Figure 22, and the deposition of particles on the heated canister surface is shown in Figure 23. The overall deposition plot shows that at low or no wind speeds the particle deposition can range from 7–20 percent. The canister deposition plot shows that not much deposition is occurring at the canister, 1 percent or less. Low flow velocities within the DCS leads to particles settling in the inlets. This settling deposition can be seen in Figure 24 for the 0.5 kW natural convection case.

The particle deposition at the canister surface increases with increasing wind speed, with the highest deposition (~ 3 percent) occurring with a wind speed of 40 mph. At 40 mph winds, the overall deposition is just under 15 percent. Figure 25 shows the particle deposition for the 5 kW heat load and 40 mph wind speed case.

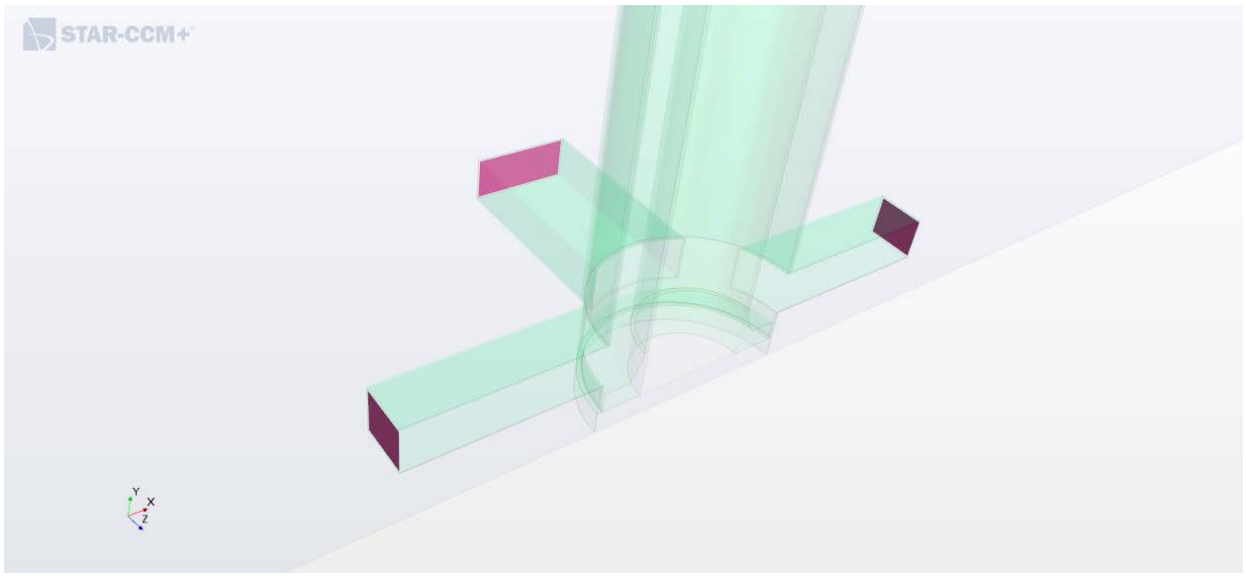

Figure 21: DCS inlet injector wind effects model – Particle injectors shown in purple.

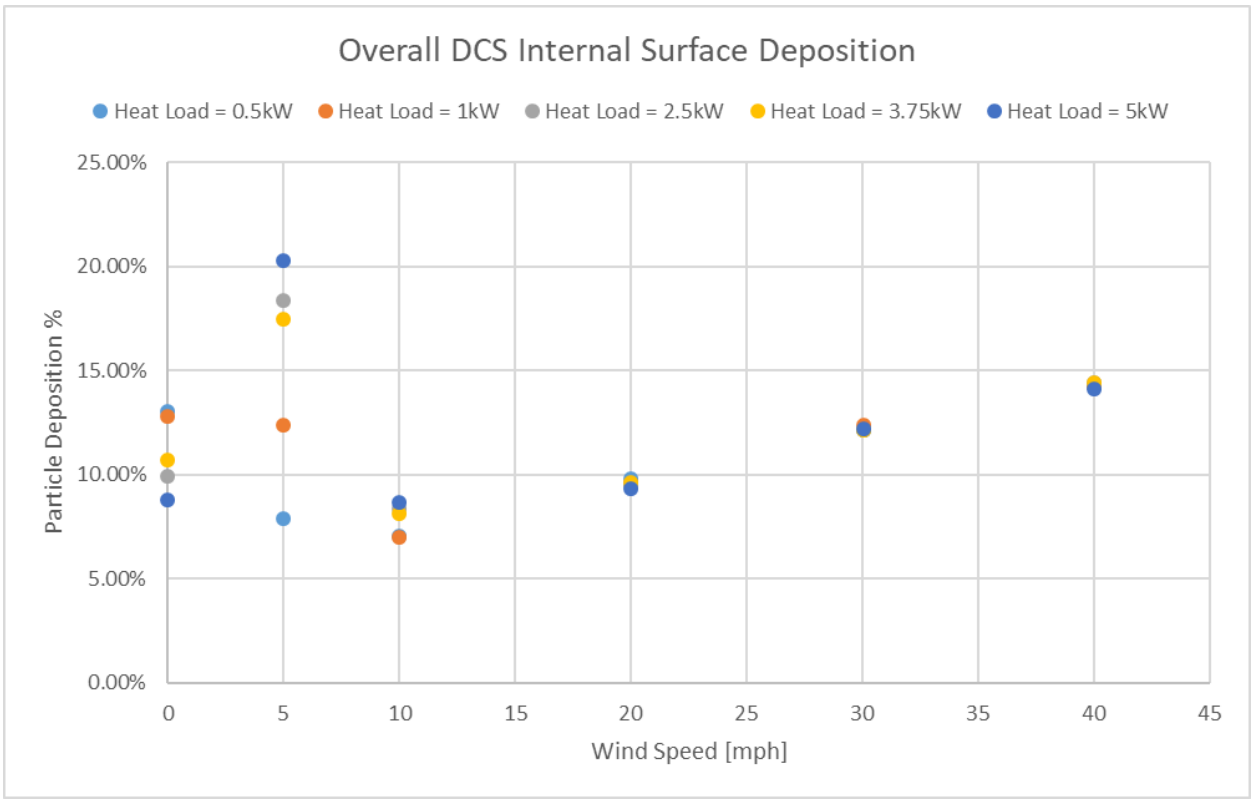

Figure 22: DCS inlet injector wind effects model – Overall particle deposition on DCS surfaces.

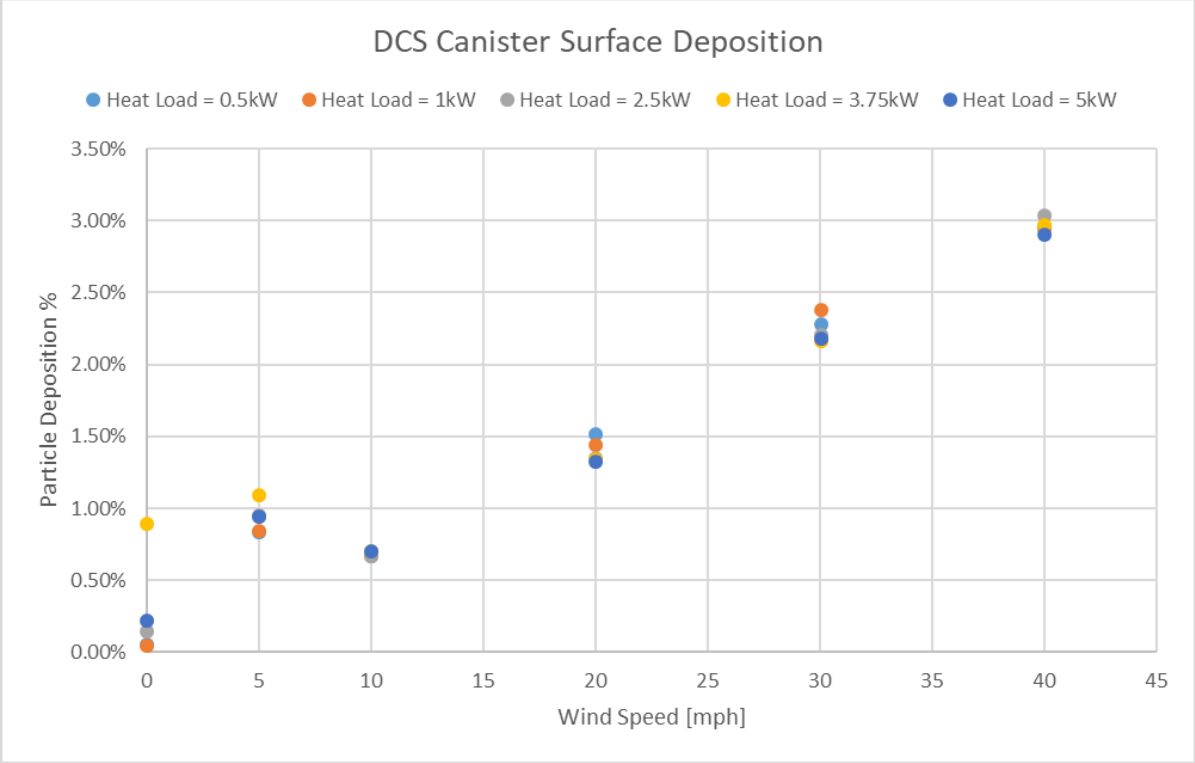

Figure 23: DCS inlet injector wind effects model – Particle deposition on canister surface.

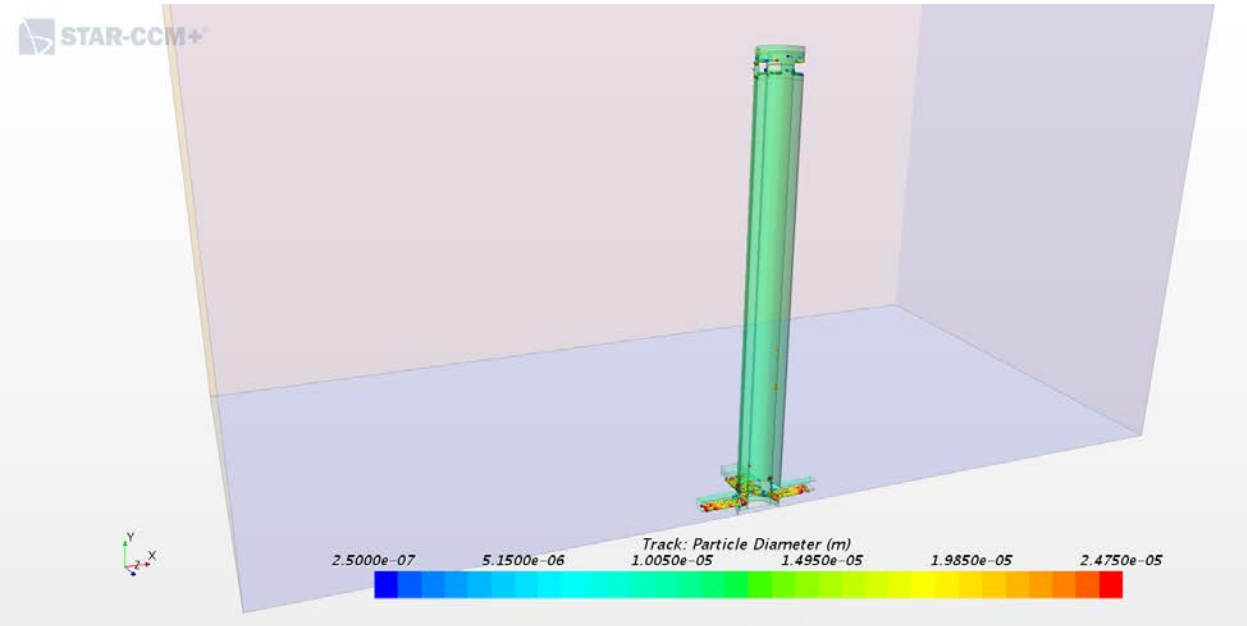

Figure 24: DCS inlet injector wind effects model @ 0.5 kW and 0 mph Wind – Size of particles deposited on DCS surfaces.

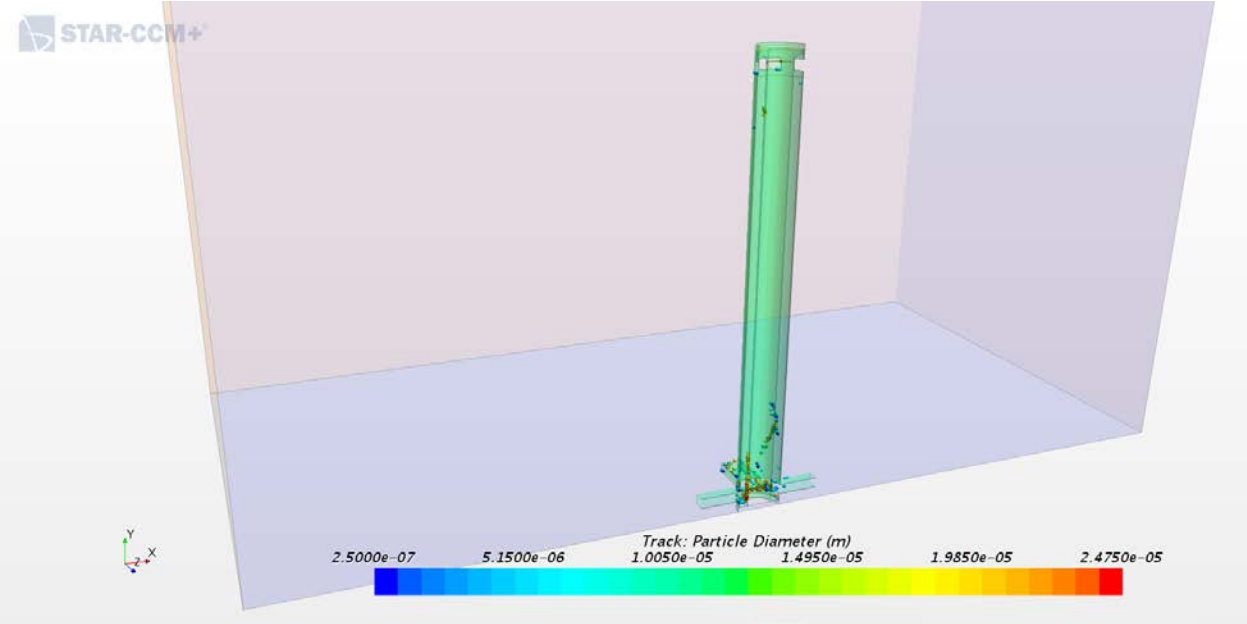

Figure 25: DCS inlet injector wind effects model @ 5 kW and 40 mph Wind – Size of particles deposited on DCS surfaces.

The inlet injector wind effects model was also used to look at the particle size distribution of deposition on the canister. Figure 26, Figure 27, Figure 28, Figure 29, Figure 30, and Figure 31 show the resulting canister deposition particle size distribution at various wind speeds. The plots show that as flow through the DCS changes, so does the particle deposition size distribution at the canister surface. The natural convection case (no wind) shows the strongest deposition dependence on heat load within a given particle diameter range. At a wind speed of 5 mph the smaller particles were more likely to deposit on the canister surface, and as the wind speed increased, the deposition of the smaller particles went down. The larger particles were more likely to deposit on the canister surface as the wind speed increased.

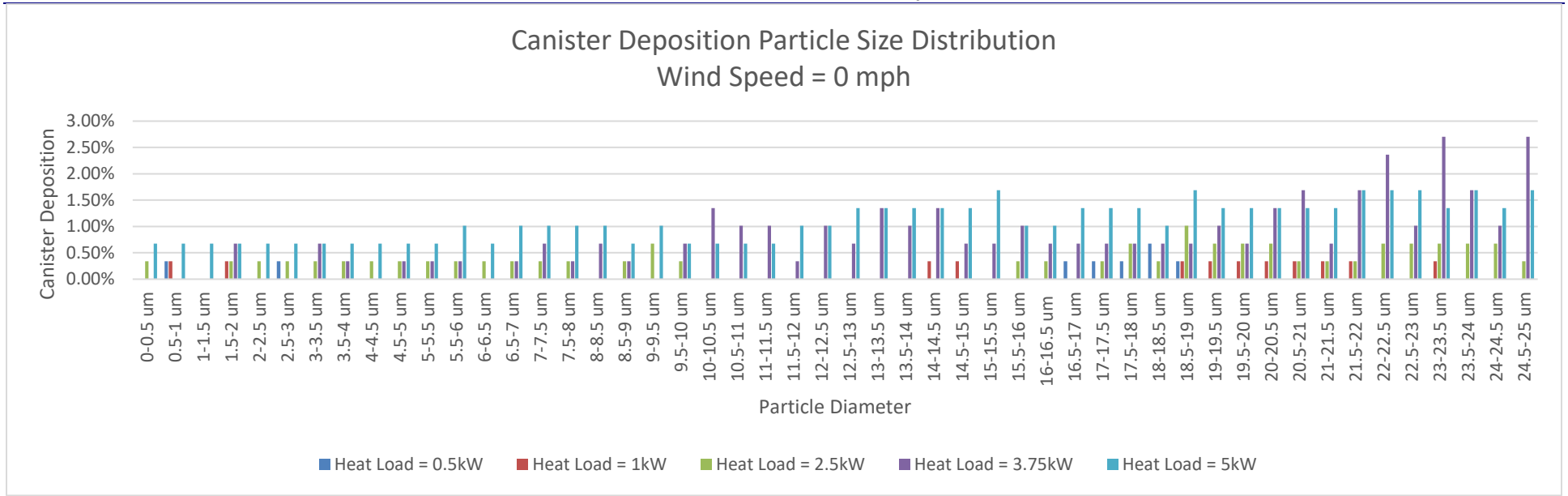

Figure 26: DCS inlet injector @ 0 mph wind – Canister deposition particle size distribution.

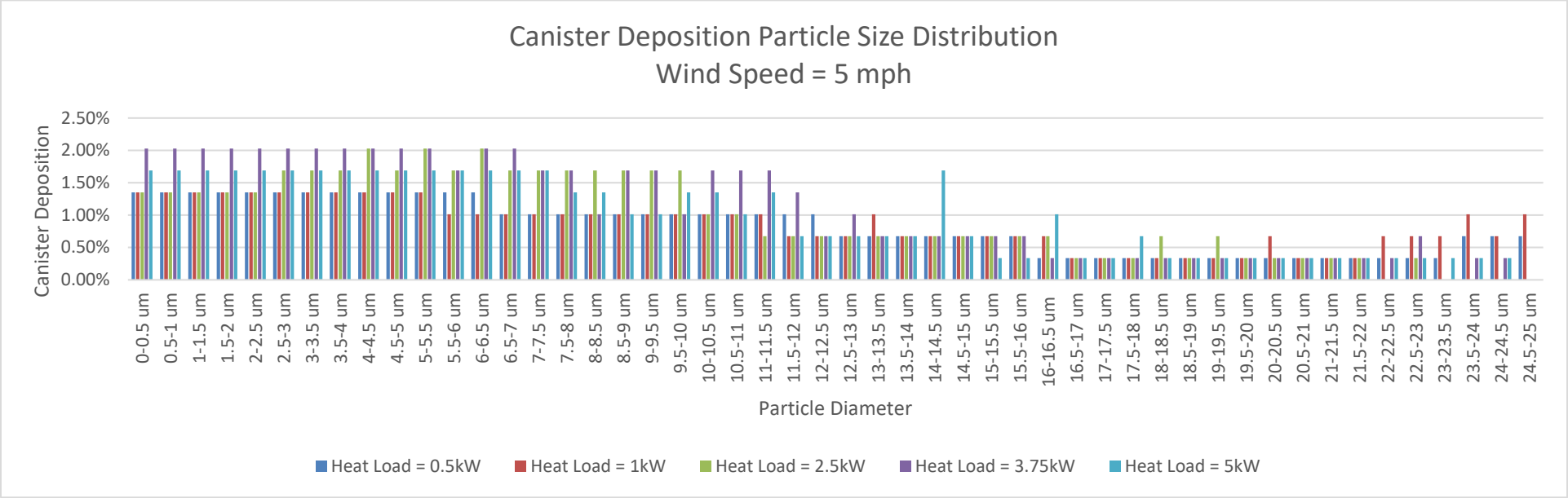

Figure 27: DCS inlet injector @ 5 mph wind – Canister deposition particle size distribution.

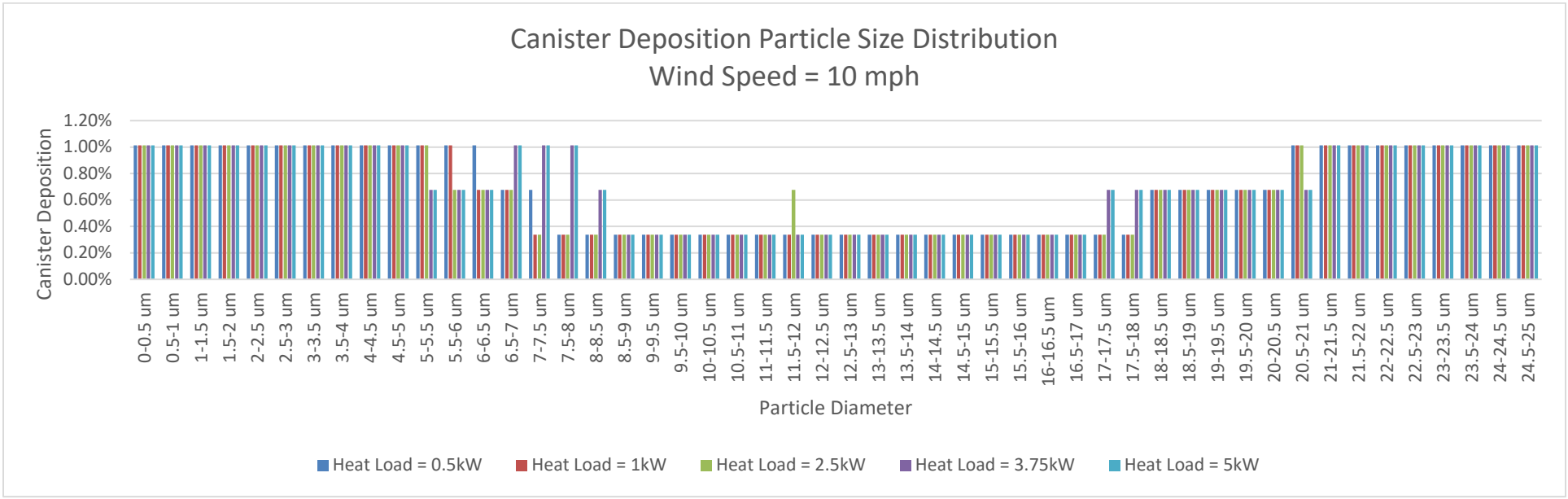

Figure 28: DCS inlet injector @ 10 mph wind – Canister deposition particle size distribution.

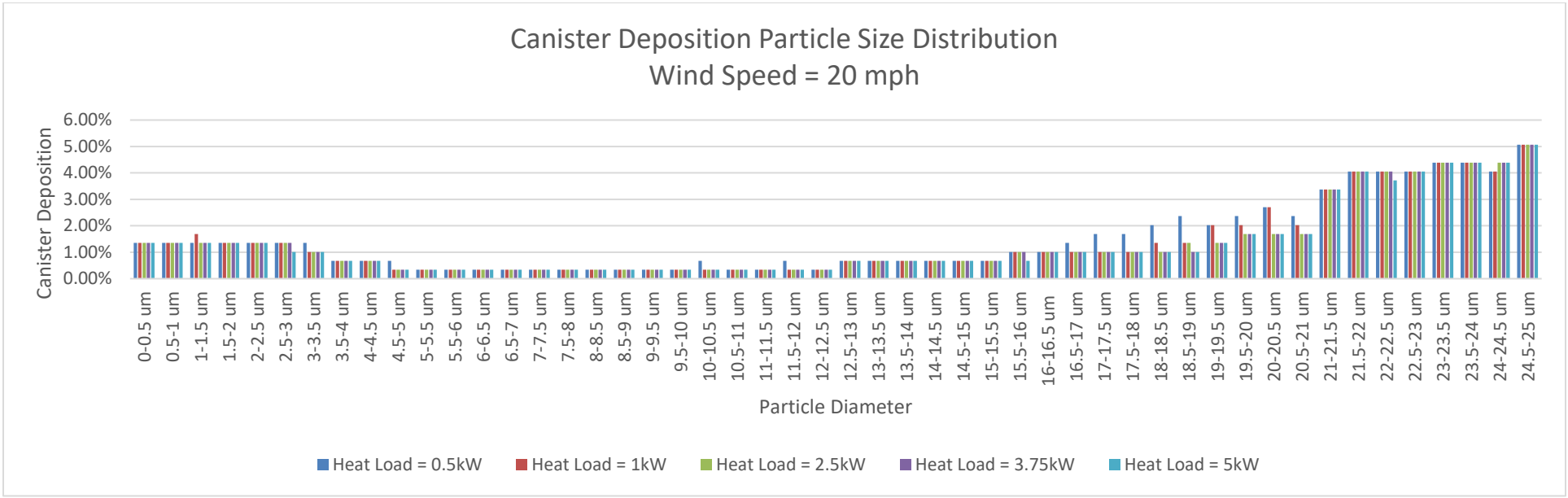

Figure 29: DCS inlet injector @ 20 mph wind – Canister deposition particle size distribution.

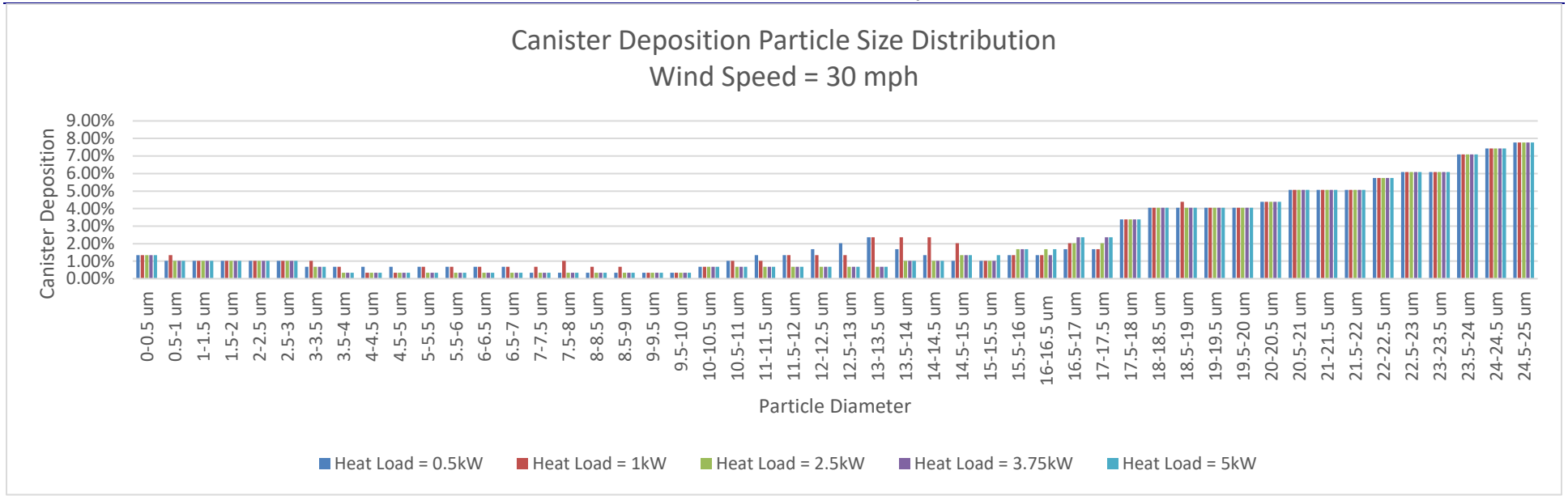

Figure 30: DCS inlet injector @ 30 mph wind – Canister deposition particle size distribution.

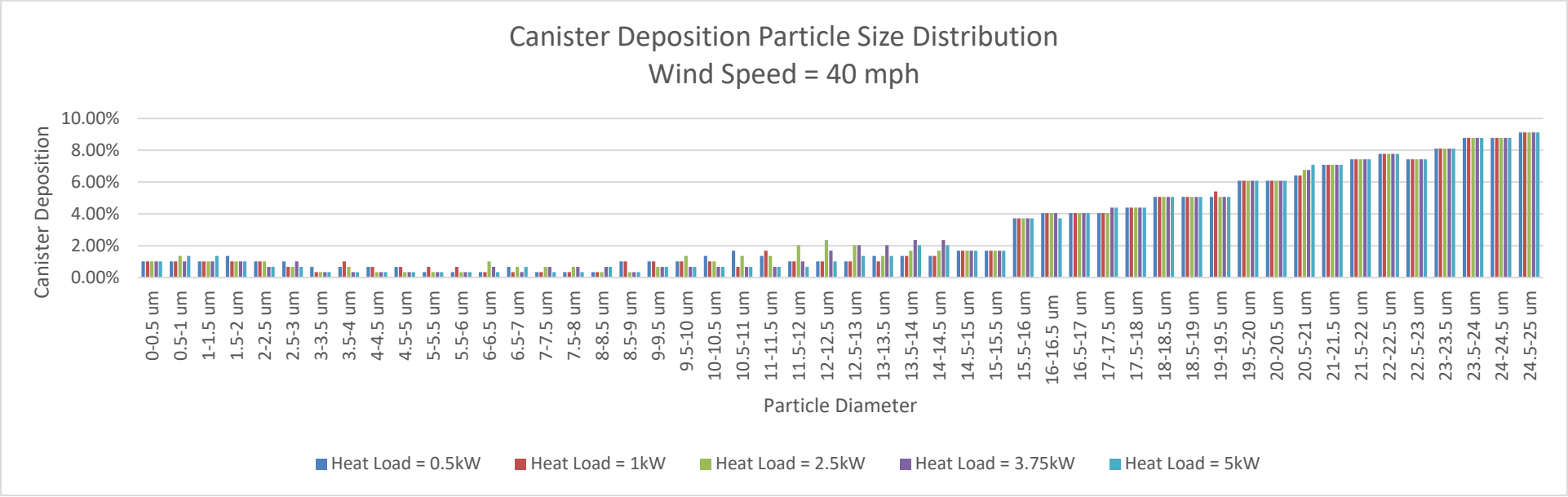

Figure 31: DCS inlet injector @ 40 mph wind – Canister deposition particle size distribution.

3.1.2.3 Inlet and Outlet Injector

The inlet injector wind effects model was modified to incorporate injectors at the outlets of the DCS. This case models the effect of driving wind, driving particles into all inlets and outlets simultaneously. This case may not be representative, but it provides useful information for better understanding how particles enter the system. These new outlet injectors were assigned the same distribution and injection rate as the inlet injectors. Figure 32 shows the locations of the outlet injectors. The overall particle deposition is plotted for various heat load and wind speed combinations in Figure 33, and the deposition of particles on the heated canister surface is shown in Figure 34. The particle deposition percentages in Figure 33 and Figure 34 are scaled using the total injected flow rate of particles. Because this simulation used both inlet and outlet injectors, the total injected flow rate of particles was double the flow rate in the inlet injector model. The amount of particle deposition was not significantly affected by the inclusion of outlet injectors, especially at wind speeds greater than 10 mph. The effects of thermophoresis are apparent when examining the canister surface deposition at low wind speeds. At higher wind speeds, thermophoresis does not appear to be an important factor in deposition rates

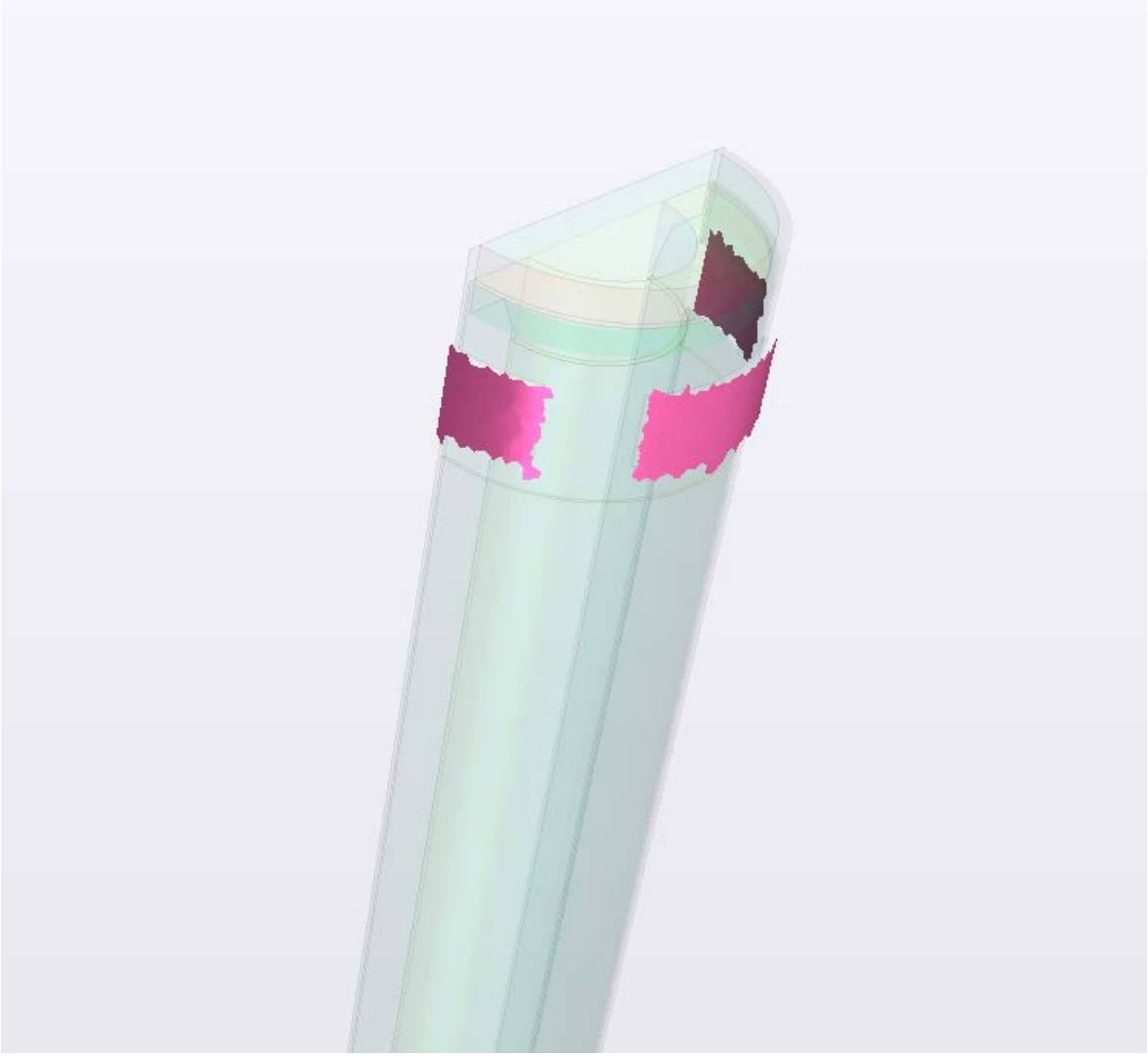

Figure 32: DCS outlet injector wind effects model – Particle injectors shown in purple.

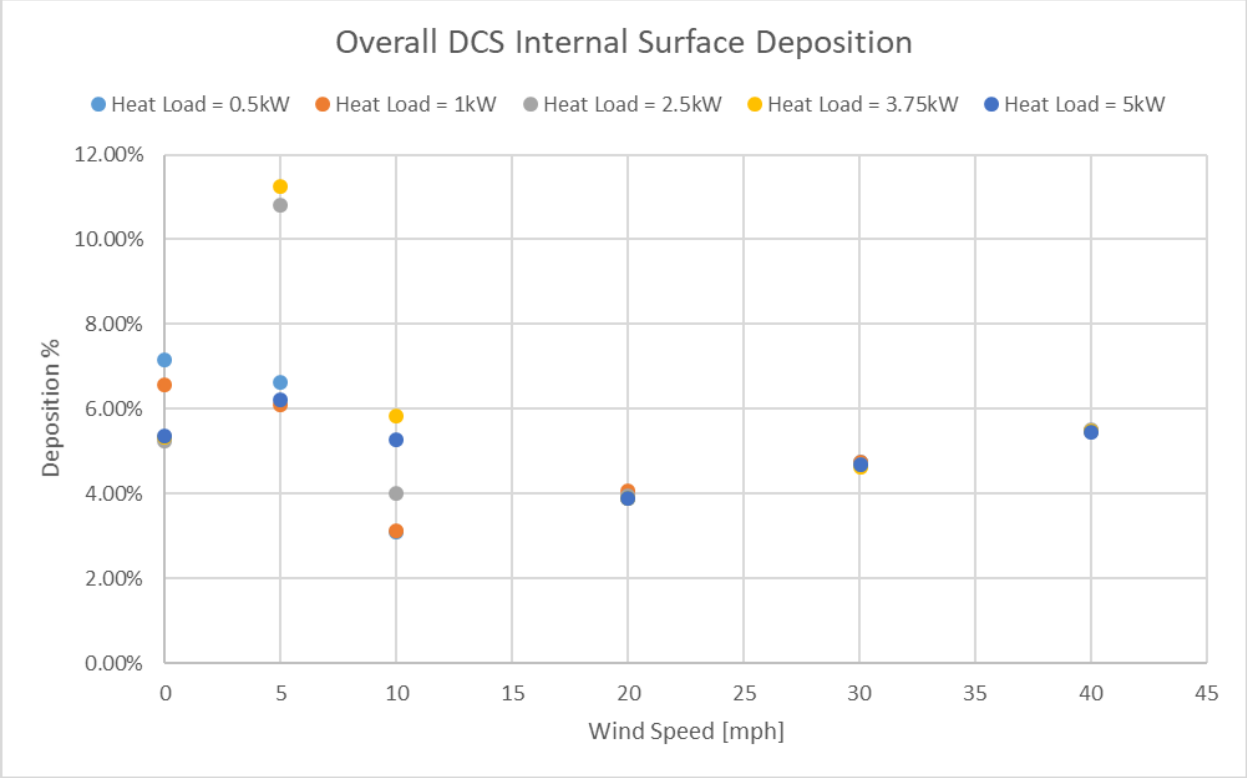

Figure 33: DCS outlet injector wind effects model – Overall particle deposition on DCS surfaces.

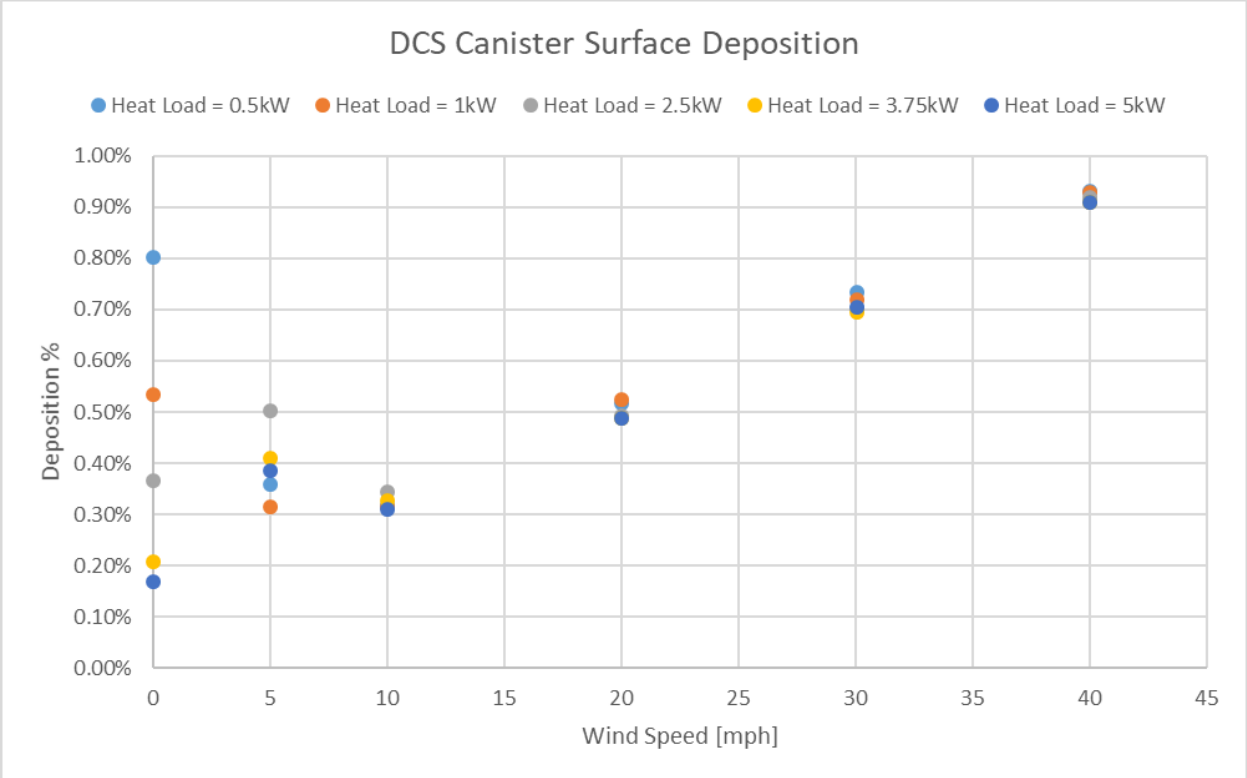

Figure 34: DCS outlet injector wind effects model – Particle deposition on canister surface.

3.2 MAGNASTOR® Model

A detailed thermal model of the NAC International MAGNASTOR® was previously developed using STAR-CCM+ (Fort et al. 2016). The model was developed to obtain temperature predictions for a loaded fuel storage cask in the Catawba ISFSI.

A 3-dimensional model of the MAGNASTOR® geometry was created in the solid modeling CAD software SolidWorks (Dassault 2017). The CAD geometry was generated from 2-dimensional drawings of the MAGNASTOR® system provided by Duke Energy. The CAD geometry is shown in Figure 35. Air enters the system at the inlets located near the base of the cask and exits at the outlets near the top of the system.

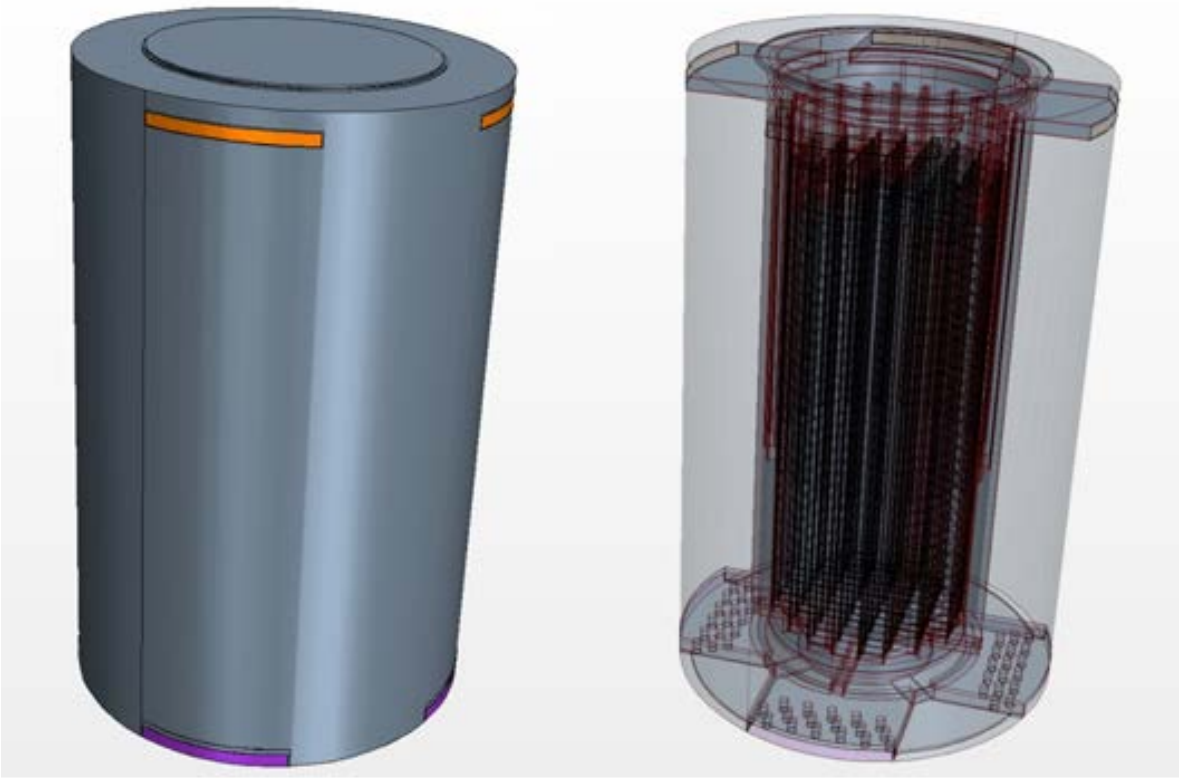

Figure 35: CAD model geometry for MAGNASTOR®.

The SolidWorks geometry was imported into STAR-CCM+. The geometry was then meshed into 77 separate regions connected by 380 interface boundaries, resulting in a single conformal volume mesh across all regions. The polyhedral volume mesh contains 6,126,939 cells, 27,338,512 faces, and 21,361,006 vertices. Along each wall/fluid interface, the mesh contains a prism layer to improve the accuracy of the flow solution near the walls. The prism layer consists of orthogonal prismatic cells, 4 cells thick, adjacent to the wall boundaries. Figure 36 and Figure 37 show the mesh assembly. A detailed description of the MAGNASTOR® model can be found in Fort et al. 2016.

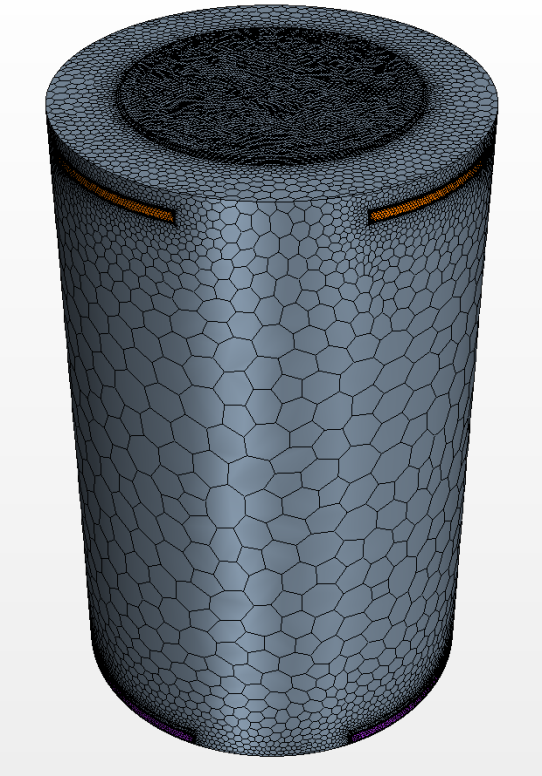

Figure 36: MAGNASTOR® concrete cask mesh.

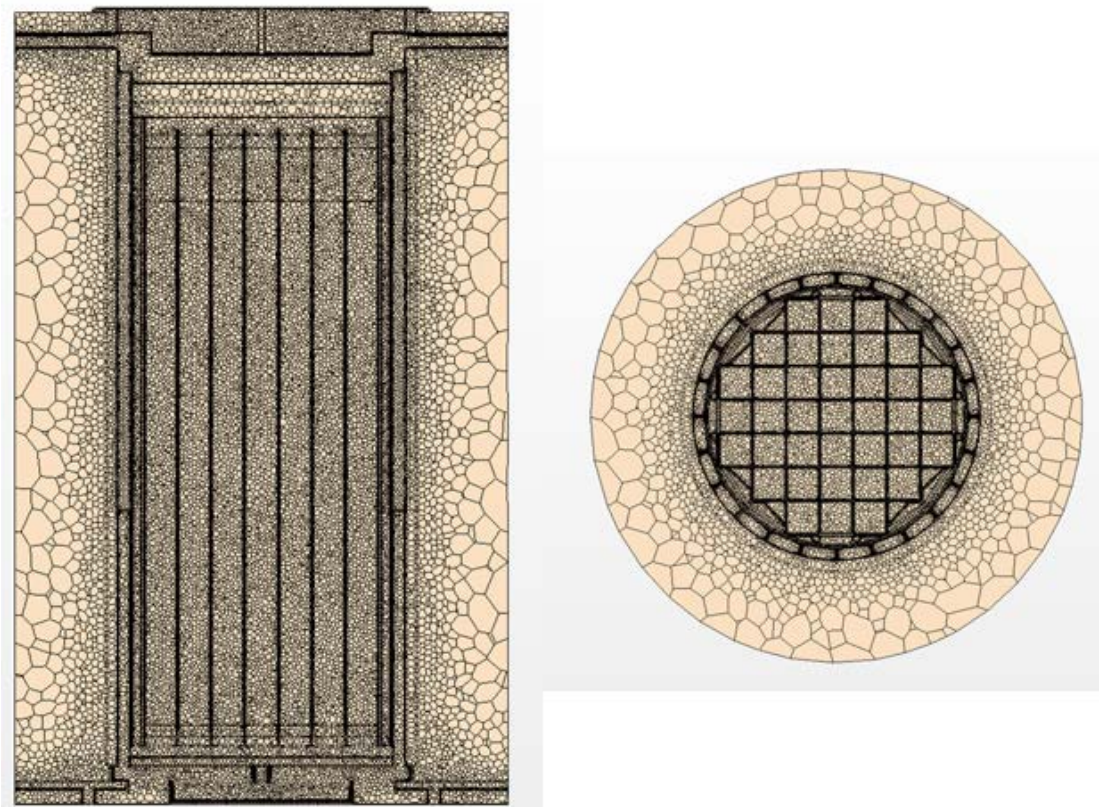

Figure 37: MAGNASTOR® mesh – Axial & radial cross-sectional view.

Particles were injected at the inlets of the MAGNASTOR® with the uniform CDF particle distribution. The particle simulations were run over a heat load range from 5–35 kW. An ambient temperature of 20°C was assumed for the external environment. The resulting overall particle deposition and canister particle deposition is shown in Figure 38. Unlike the DCS, the MAGNASTOR® model has a plenum space above the canister that allows a significant number of particles to be deposited on the top of the canister. A large number of particles also deposited on the inlet and outlets. Figure 39 and Figure 40 show the particles stuck at the boundaries and the corresponding particle diameter of the stuck particles.

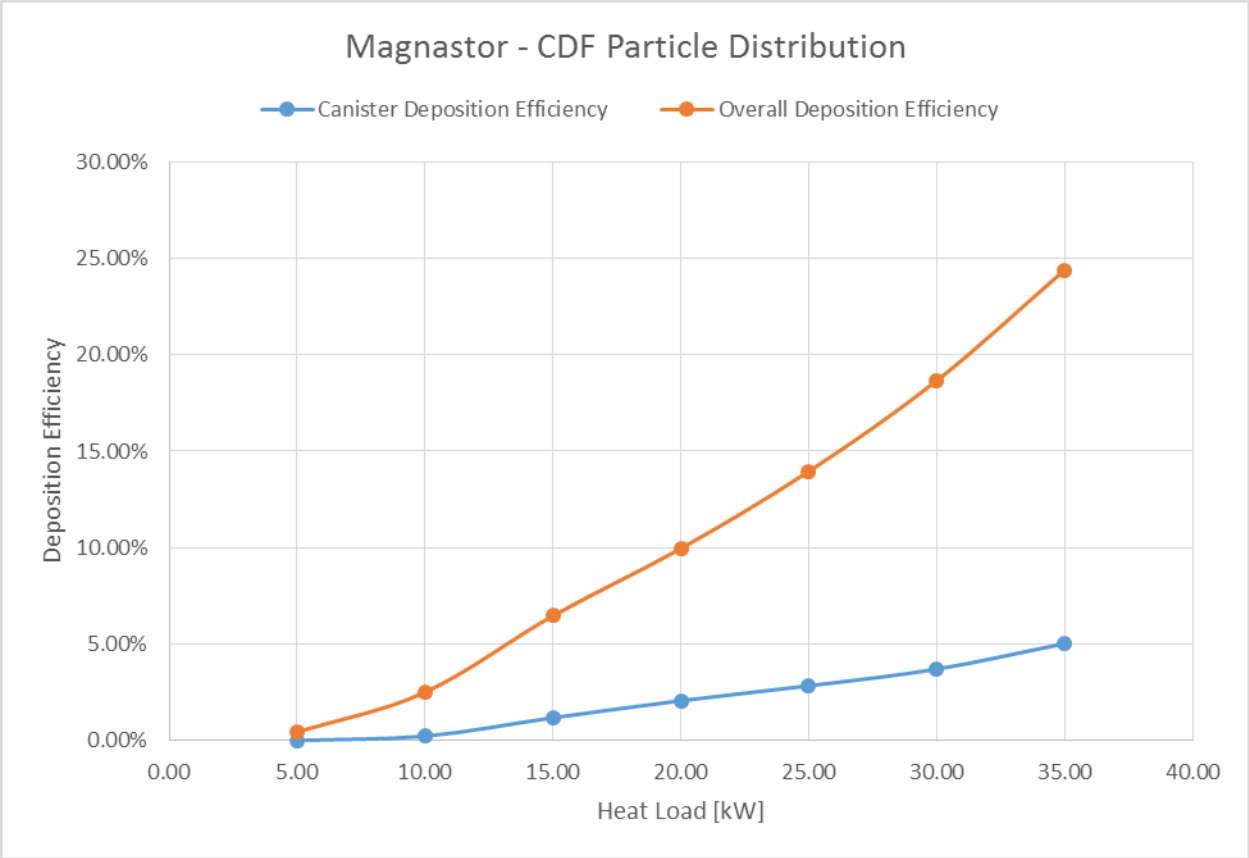

Figure 38: MAGNASTOR® model – Resulting particle deposition for a CDF particle distribution.

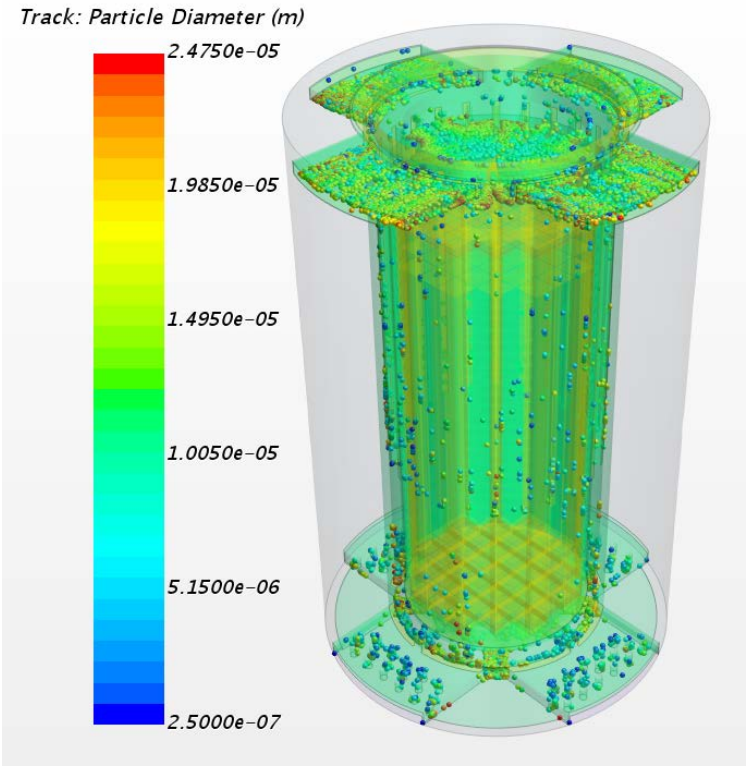

Figure 39: MAGNASTOR® model – Stuck particles at the boundaries.

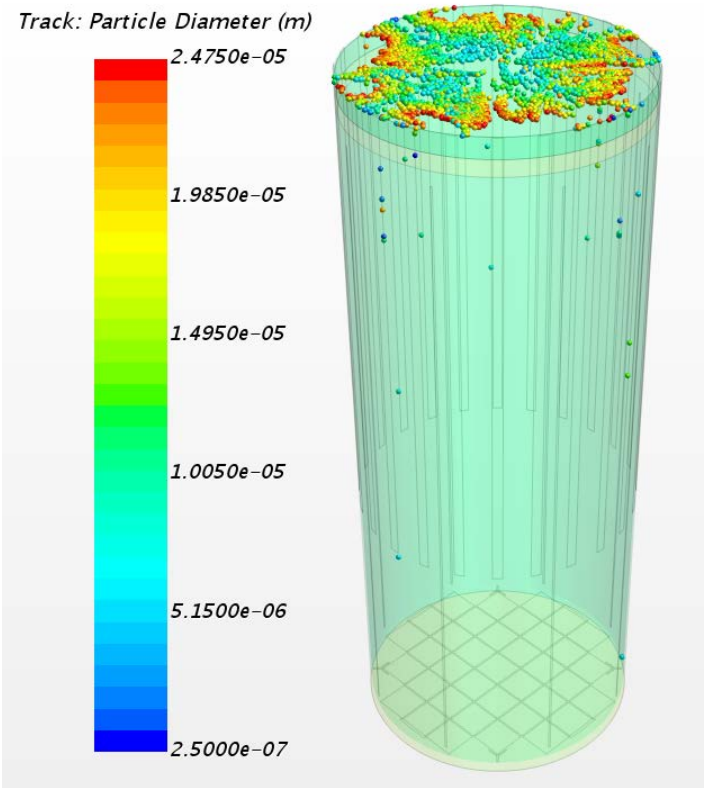

Figure 40: MAGNASTOR® model – Stuck particles at the canister surfaces.

Detailed results showing the deposition results for individual components of the MAGNASTOR® system are shown in Table 1. Figure 41 shows the naming convention used for each component of the Maganstor system. Table 1 shows that the majority of the particles that enter the system exit the system without depositing on a surface. Of the particles that do deposit, the majority deposit at the inlet. The key results for the dry shielded canister (DSC) show that most of the material deposited on the canister is deposited on the lid. Very little material is deposited on the canister walls.

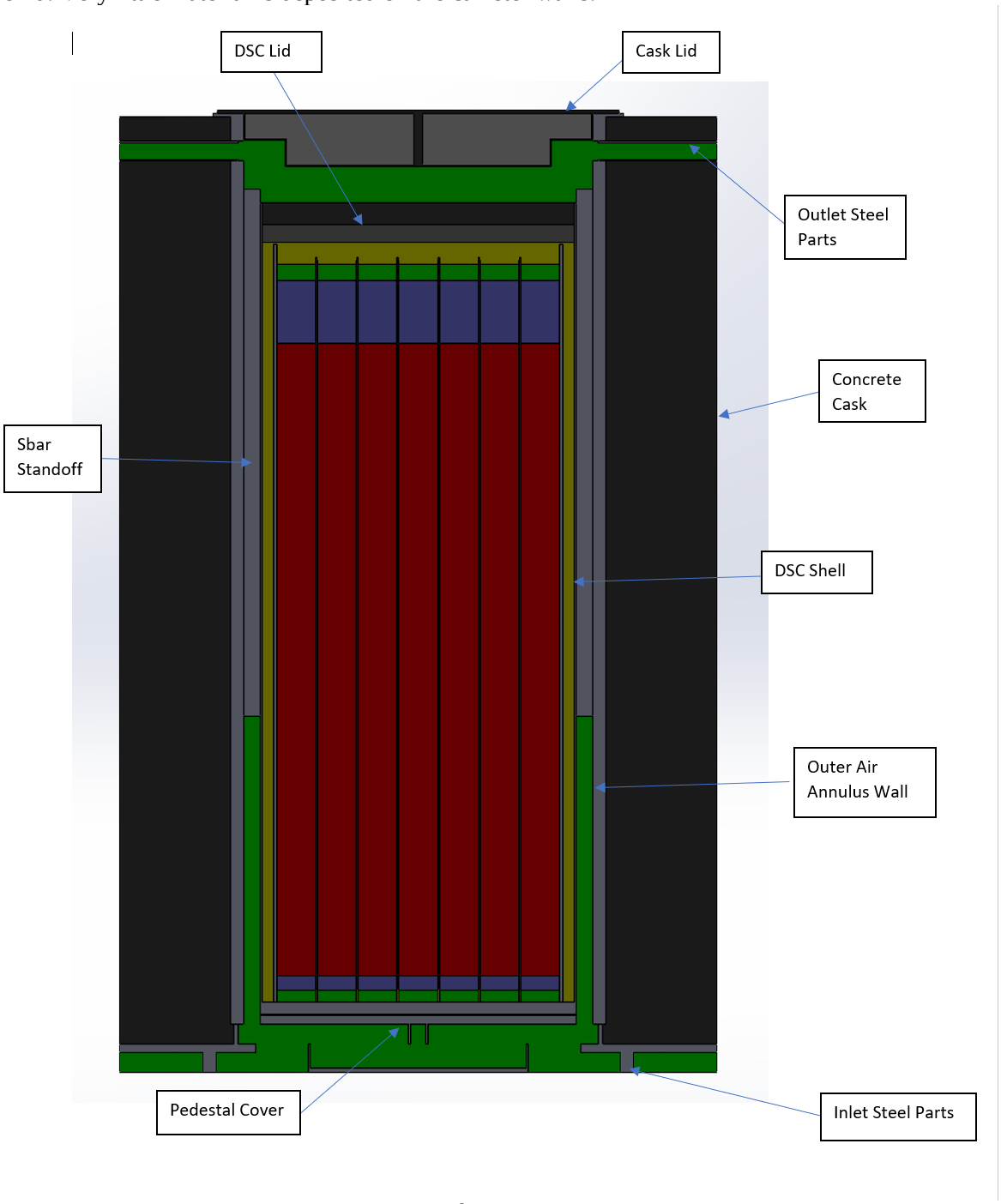

Figure 41: MAGNASTOR® component naming convention.

Table 1: MAGNASTOR® detailed deposition results.

Boundary	Heat Load [kW]	Particle Thermal Conductivity [W/m-K]	Avg Surface Temp [C]	Max Surface Temp [C]	Avg Inlet Velocity [m/s]	Avg Annulus Velocity [m/s]	Min Stuck Particle Diameter [m]	Max Stuck Particle Diameter [m]	Inlet Mass Flowrate [kg/s]	Stuck Mass Flowrate [kg/s]	DSC Deposition Efficiency	Deposition Efficiency
Concrete Cask (concrete)	5	0.613	32.66	35.41	0.25	0.07	8.75E-06	1.83E-05	1.65E-10	3.53E-15		0.00%
Cask Lid (carbon steel)	5	0.613	86.92	94.74	0.25	0.07	2.50E-07	9.25E-06	1.65E-10	7.96E-16		0.00%
Outer Air Annulus Wall (carbon steel)	5	0.613	83.34	102.42	0.25	0.07	2.50E-07	1.58E-05	1.65E-10	4.65E-14		0.03%
Inlet Steel Parts (carbon steel)	5	0.613	49.65	64.24	0.25	0.07	2.50E-07	1.98E-05	1.65E-10	5.60E-13		0.34%
DSC Lid (carbon steel)	5	0.613	106.47	108.96	0.25	0.07	7.50E-07	1.13E-05	1.65E-10	2.79E-14		0.02%
Outlet Steel Parts (carbon steel)	5	0.613	70.06	92.16	0.25	0.07	2.50E-07	1.38E-05	1.65E-10	5.26E-14		0.03%
Pedestal Cover (stainless steel)	5	0.613	63.63	64.31	0.25	0.07	-	-	1.65E-10	0		0.00%
Sbar Standoffs (carbon steel)	5	0.613	99.76	107.16	0.25	0.07	2.50E-07	1.33E-05	1.65E-10	2.86E-14		0.02%
DSC Shell (stainless steel)	5	0.613	95.15	112.26	0.25	0.07	2.50E-07	8.75E-06	1.65E-10	2.92E-15	0.02%	0.00%
Total Air Boundaries	5	0.613	-	-	0.25	0.07	2.50E-07	1.98E-05	1.65E-10	7.23E-13		0.44%
Concrete Cask (concrete)	10	0.613	31.70	34.21	0.27	0.12	-	-	1.57E-10	0.00E+00		0.00%
Cask Lid (carbon steel)	10	0.613	108.52	121.56	0.27	0.12	2.50E-07	4.75E-06	1.57E-10	6.51E-16		0.00%
Outer Air Annulus Wall (carbon steel)	10	0.613	96.16	126.14	0.27	0.12	2.50E-07	2.08E-05	1.57E-10	4.52E-13		0.29%
Inlet Steel Parts (carbon steel)	10	0.613	52.18	72.24	0.27	0.12	2.50E-07	2.18E-05	1.57E-10	2.42E-12		1.54%
DSC Lid (carbon steel)	10	0.613	137.35	141.61	0.27	0.12	2.25E-06	2.03E-05	1.57E-10	3.82E-13		0.24%
Outlet Steel Parts (carbon steel)	10	0.613	81.40	114.43	0.27	0.12	2.50E-07	1.53E-05	1.57E-10	5.34E-13		0.34%
Pedestal Cover (stainless steel)	10	0.613	71.32	72.14	0.27	0.12	-	-	1.57E-10	0		0.00%
Sbar Standoffs (carbon steel)	10	0.613	121.26	137.53	0.27	0.12	2.50E-07	1.53E-05	1.57E-10	1.60E-13		0.10%
DSC Shell (stainless steel)	10	0.613	114.36	145.94	0.27	0.12	3.25E-06	1.18E-05	1.57E-10	2.60E-14	0.26%	0.02%
Total Air Boundaries	10	0.613	-	-	0.27	0.12	2.50E-07	2.18E-05	1.57E-10	3.97E-12		2.53%
Concrete Cask (concrete)	15	0.613	31.91	34.50	0.27	0.18	-	-	1.62E-10	0.00E+00		0.00%
Cask Lid (carbon steel)	15	0.613	126.16	143.71	0.27	0.18	7.50E-07	1.28E-05	1.62E-10	2.95E-14		0.02%
Outer Air Annulus Wall (carbon steel)	15	0.613	107.46	145.62	0.27	0.18	2.50E-07	2.43E-05	1.62E-10	1.20E-12		0.74%
Inlet Steel Parts (carbon steel)	15	0.613	56.77	82.39	0.27	0.18	2.50E-07	2.43E-05	1.62E-10	5.94E-12		3.65%
DSC Lid (carbon steel)	15	0.613	162.22	168.41	0.27	0.18	1.75E-06	2.48E-05	1.62E-10	1.28E-12		0.79%
Outlet Steel Parts (carbon steel)	15	0.613	92.75	132.65	0.27	0.18	2.50E-07	2.28E-05	1.62E-10	2.29E-12		1.41%
Pedestal Cover (stainless steel)	15	0.613	81.10	82.25	0.27	0.18	-	-	1.62E-10	0		0.00%
Sbar Standoffs (carbon steel)	15	0.613	138.47	161.72	0.27	0.18	2.50E-07	1.58E-05	1.62E-10	2.36E-13		0.15%
DSC Shell (stainless steel)	15	0.613	131.43	173.01	0.27	0.18	7.50E-07	1.63E-05	1.62E-10	3.40E-14	1.43%	0.02%
Total Air Boundaries	15	0.613	-	-	0.27	0.18	2.50E-07	2.48E-05	1.62E-10	1.10E-11		6.78%
Concrete Cask (concrete)	20	0.613	32.38	35.26	0.28	0.22	-	-	1.60E-10	0.00E+00		0.00%
Cask Lid (carbon steel)	20	0.613	141.83	163.01	0.28	0.22	2.50E-07	5.75E-06	1.60E-10	9.08E-16		0.00%
Outer Air Annulus Wall (carbon steel)	20	0.613	118.17	162.74	0.28	0.22	2.50E-07	2.18E-05	1.60E-10	1.23E-12		0.77%
Inlet Steel Parts (carbon steel)	20	0.613	61.67	92.54	0.28	0.22	2.50E-07	2.48E-05	1.60E-10	9.50E-12		5.93%
DSC Lid (carbon steel)	20	0.613	184.00	192.51	0.28	0.22	2.75E-06	2.43E-05	1.60E-10	3.67E-12		2.29%
Outlet Steel Parts (carbon steel)	20	0.613	103.59	147.80	0.28	0.22	1.25E-06	2.13E-05	1.60E-10	2.82E-12		1.76%
Pedestal Cover (stainless steel)	20	0.613	90.85	92.18	0.28	0.22	-	-	1.60E-10	0		0.00%
Sbar Standoffs (carbon steel)	20	0.613	154.06	183.44	0.28	0.22	2.50E-07	2.08E-05	1.60E-10	3.83E-13		0.24%
DSC Shell (stainless steel)	20	0.613	147.36	197.60	0.28	0.22	2.75E-06	1.33E-05	1.60E-10	1.72E-14	2.30%	0.01%
Total Air Boundaries	20	0.613	-	-	0.28	0.22	2.50E-07	2.48E-05	1.60E-10	1.76E-11		11.00%
Concrete Cask (concrete)	25	0.613	32.85	35.92	0.28	0.27	-	-	1.58E-10	0.00E+00		0.00%
Cask Lid (carbon steel)	25	0.613	155.57	180.77	0.28	0.27	2.50E-07	9.75E-06	1.58E-10	1.41E-15		0.00%
Outer Air Annulus Wall (carbon steel)	25	0.613	128.40	178.73	0.28	0.27	2.50E-07	2.48E-05	1.58E-10	1.20E-12		0.76%
Inlet Steel Parts (carbon steel)	25	0.613	66.36	102.16	0.28	0.27	2.50E-07	2.48E-05	1.58E-10	9.71E-12		6.13%
DSC Lid (carbon steel)	25	0.613	204.14	214.42	0.28	0.27	2.50E-07	2.48E-05	1.58E-10	4.54E-12		2.87%
Outlet Steel Parts (carbon steel)	25	0.613	112.13	161.08	0.28	0.27	2.50E-07	2.48E-05	1.58E-10	6.20E-12		3.92%
Pedestal Cover (stainless steel)	25	0.613	100.04	101.85	0.28	0.27	-	-	1.58E-10	0		0.00%
Sbar Standoffs (carbon steel)	25	0.613	168.59	203.05	0.28	0.27	2.50E-07	2.38E-05	1.58E-10	3.49E-13		0.22%
DSC Shell (stainless steel)	25	0.613	162.38	219.30	0.28	0.27	2.50E-07	1.78E-05	1.58E-10	2.67E-14	2.89%	0.02%
Total Air Boundaries	25	0.613	-	-	0.28	0.27	2.50E-07	2.48E-05	1.58E-10	2.20E-11		13.91%
Concrete Cask (concrete)	30	0.613	33.33	36.62	0.29	0.31	1.18E-05	1.18E-05	1.64E-10	6.06E-15		0.00%
Cask Lid (carbon steel)	30	0.613	169.32	198.92	0.29	0.31	1.25E-06	6.25E-06	1.64E-10	1.09E-15		0.00%
Outer Air Annulus Wall (carbon steel)	30	0.613	138.35	193.70	0.29	0.31	2.50E-07	2.48E-05	1.64E-10	2.48E-12		1.51%
Inlet Steel Parts (carbon steel)	30	0.613	70.69	111.12	0.29	0.31	2.50E-07	2.48E-05	1.64E-10	1.33E-11		8.12%
DSC Lid (carbon steel)	30	0.613	223.32	235.81	0.29	0.31	3.75E-06	2.48E-05	1.64E-10	6.45E-12		3.94%
Outlet Steel Parts (carbon steel)	30	0.613	119.40	173.48	0.29	0.31	2.50E-07	2.48E-05	1.64E-10	1.04E-11		6.35%
Pedestal Cover (stainless steel)	30	0.613	108.20	110.47	0.29	0.31	-	-	1.64E-10	0		0.00%
Sbar Standoffs (carbon steel)	30	0.613	182.55	221.79	0.29	0.31	2.50E-07	2.48E-05	1.64E-10	8.14E-13		0.50%
DSC Shell (stainless steel)	30	0.613	176.76	240.58	0.29	0.31	5.75E-06	8.25E-06	1.64E-10	6.53E-15	3.94%	0.00%
Total Air Boundaries	30	0.613	-	-	0.29	0.31	2.50E-07	2.48E-05	1.64E-10	3.34E-11		20.43%
Concrete Cask (concrete)	35	0.613	33.98	37.42	0.30	0.36	2.50E-07	2.43E-05	1.71E-10	5.50E-15		0.00%
Cask Lid (carbon steel)	35	0.613	184.05	217.91	0.30	0.36	2.50E-07	2.48E-05	1.71E-10	4.47E-14		0.03%
Outer Air Annulus Wall (carbon steel)	35	0.613	149.05	209.26	0.30	0.36	2.50E-07	2.48E-05	1.71E-10	2.43E-12		1.43%
Inlet Steel Parts (carbon steel)	35	0.613	75.26	120.24	0.30	0.36	2.50E-07	2.48E-05	1.71E-10	1.43E-11		8.41%
DSC Lid (carbon steel)	35	0.613	243.09	257.92	0.30	0.36	2.50E-07	2.48E-05	1.71E-10	8.50E-12		4.99%
Outlet Steel Parts (carbon steel)	35	0.613	126.74	186.19	0.30	0.36	2.50E-07	2.48E-05	1.71E-10	1.52E-11		8.94%
Pedestal Cover (stainless steel)	35	0.613	116.61	119.00	0.30	0.36	-	-	1.71E-10	0		0.00%
Sbar Standoffs (carbon steel)	35	0.613	197.25	241.64	0.30	0.36	2.50E-07	2.48E-05	1.71E-10	6.04E-13		0.35%
DSC Shell (stainless steel)	35	0.613	191.79	262.41	0.30	0.36	2.50E-07	2.48E-05	1.71E-10	9.63E-14	5.04%	0.06%
Total Air Boundaries	35	0.613	-	-	0.30	0.36	2.50E-07	2.48E-05	1.71E-10	4.13E-11		24.21%

3.3 NUHOMS® Calvert Cliffs Model

A detailed thermal model of a NUHOMS® horizontal storage system at Calvert Cliffs was previously developed using STAR-CCM+ (Suffield et al. 2012). The thermal model was developed to yield realistic temperature predictions to support visual inspections and temperature measurements performed on two storage models in the Calvert Cliffs Nuclear Power Station's ISFSI. The specific module represented in the STAR-CCM+ model is HSM-15, an inner module in a 2x6 array of modules.

The SolidWorks® model of the HSM-15 storage module provided by EPRI is shown in Figure 42 (The DSC is not shown in this image, for clarity.). The concrete walls are imaged in semi-transparent grey, to illustrate the module internals, including the inlet and outlet airflow vents, DSC support structures, and thin steel sheets of shielding on the side walls and ceiling, which protect the concrete walls from the thermal load due to the DSC. This model was modified to include the interior structure of the DSC, consisting of the spacer disks, tie rods, fuel assemblies, and the detailed structure of the DSC top and bottom end caps. A 3-dimensional geometry of the 24P DSC (containing 24 pressurized water reactor spent fuel assemblies) was generated in SolidWorks®, and is shown in Figure 43. The 24P DSC was integrated into the SolidWorks® model of the HSM-15 storage module. The overall assembly was then used to create the fluid regions within the module and canister. This included an air region within the storage module and external to the DSC, and a helium-filled region within the DSC.

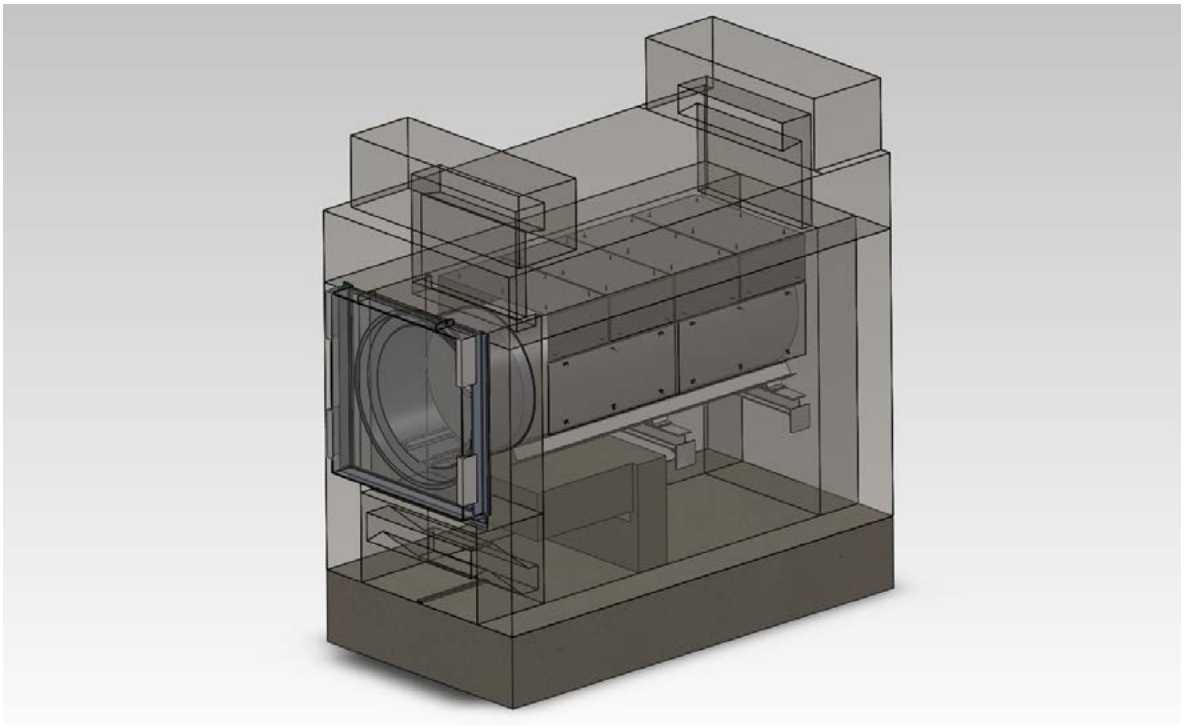

Figure 42: CAD geometry of NUHOMS® HSM-15 storage module developed by EPRI.

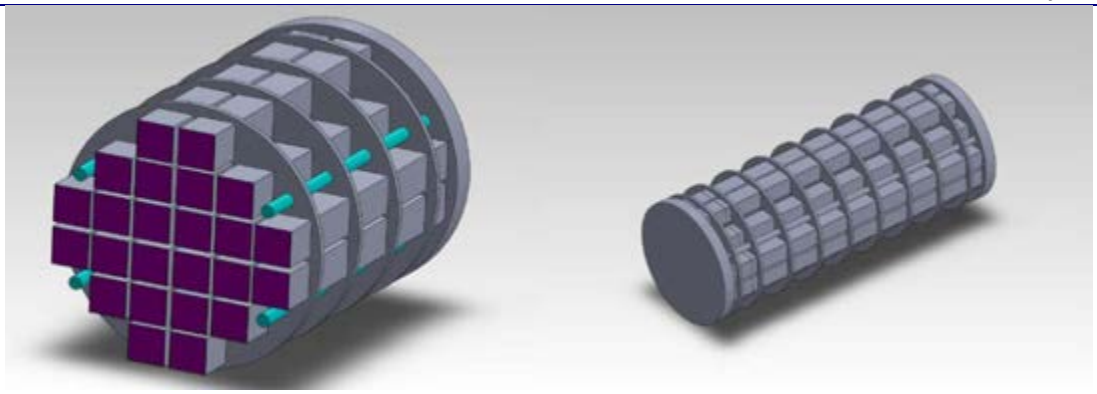

Figure 43: Mid-plane cross-sectional view and exterior view of internal geometry in SolidWorks® Model of 24P DSC.

The complete CAD model developed in SolidWorks® was imported into STAR-CCM+. The geometry was then meshed into 43 separate regions connected by 117 interface boundaries, resulting in a single conformal volume mesh across all regions. The polyhedral volume mesh of the HSM-15 module contains 21,536,624 cells, 127,598,563 faces, and 106,295,728 vertices. Along each wall/fluid interface, the mesh contains a prism layer to improve the accuracy of the flow solution near the walls. The prism layer consists of orthogonal prismatic cells, two cells thick, adjacent to the wall boundaries. Figure 44 shows an exterior view of the overall volume mesh of the HSM-15 module.

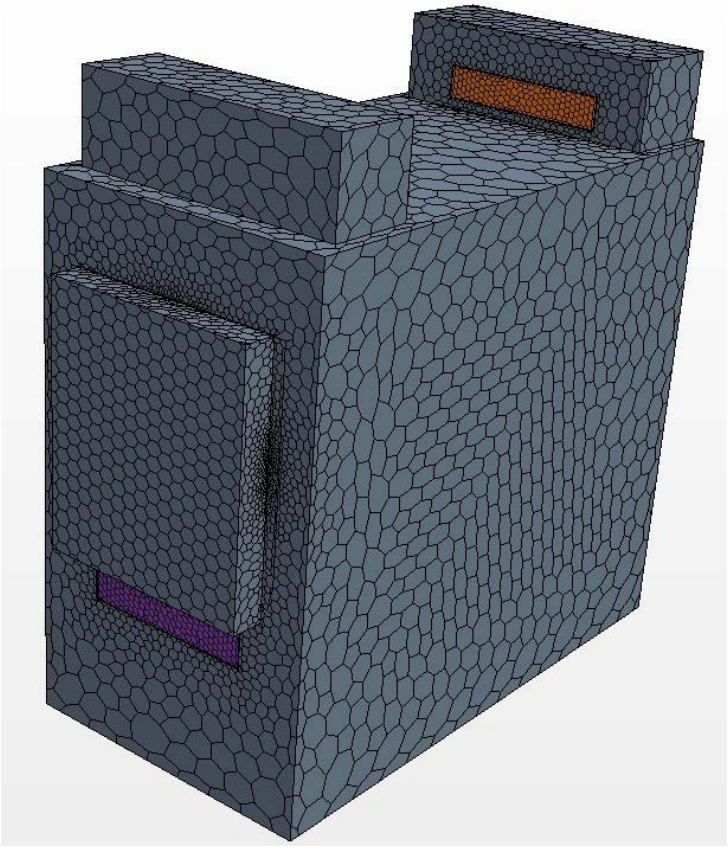

Figure 44: Volume mesh of HSM-15 module: exterior view.

Particles were injected at the inlet of the NUHOMS® HSM-15 with the uniform CDF particle distribution. The particle simulations were run over a heat load range from 5–35 kW and an ambient temperature of 20°C. The resulting particle deposition is shown in Figure 45. Results show that as the heat load and

internal surface temperatures increase, the overall deposition and canister deposition decrease. Figure 46, Figure 47, and Figure 48 compare plots of the canister temperature, particle velocity, particle deposition, and canister deposition at the 5 kW and 35 kW heat load conditions. The particle velocity plots show that the peak velocity inside the NUHOMS® model was close to double for the 35 kW heat load versus the 5 kW heat load. The canister deposition plots show less deposition at the 35 kW heat load, and that deposition occurs near the cooler end of the canister. This would indicate that thermophoresis forces push the particles away from the canister surface along the high heat sections. All canister deposition occurred near the top of the horizontal cylinder surface regardless of the heat load.

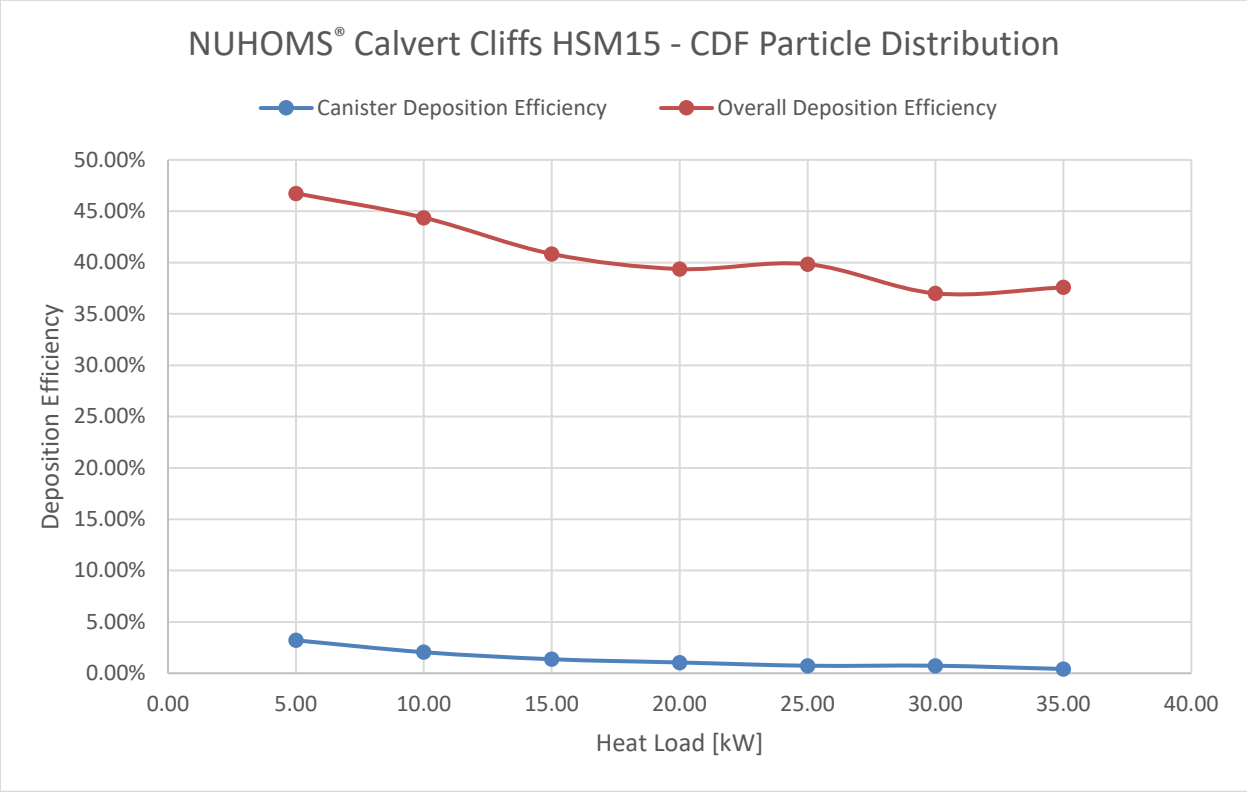

Figure 45: Resulting particle deposition for NUHOMS® Calvert Cliffs HSM-15.

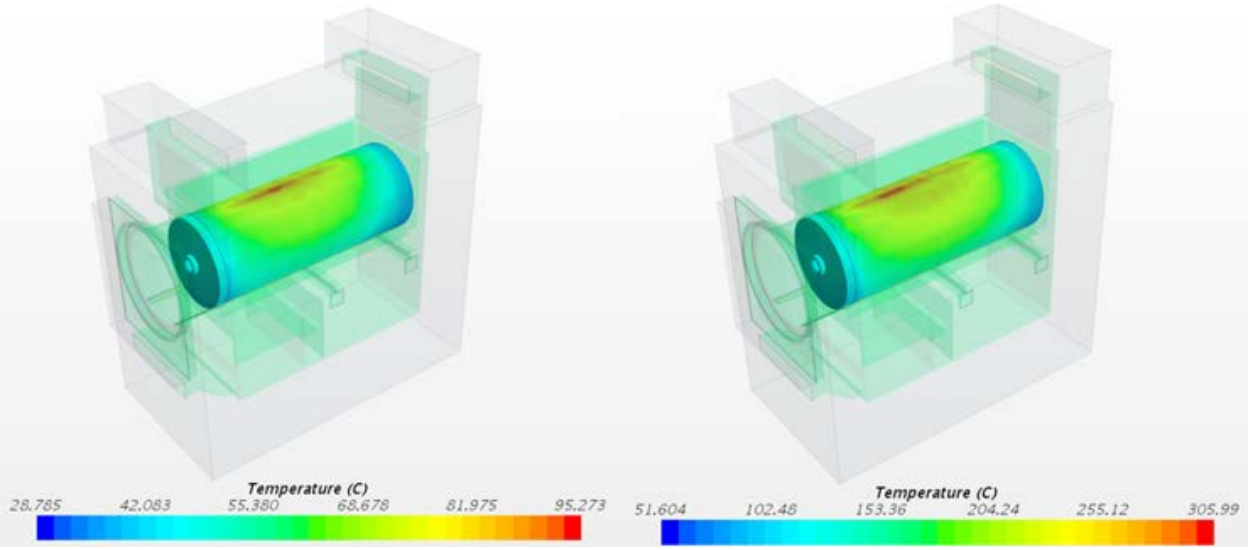

Figure 46: Canister temperature for NUHOMS® Calvert Cliffs HSM-15: 5 kW heat load shown on the left and 35 kW heat load shown on the right.

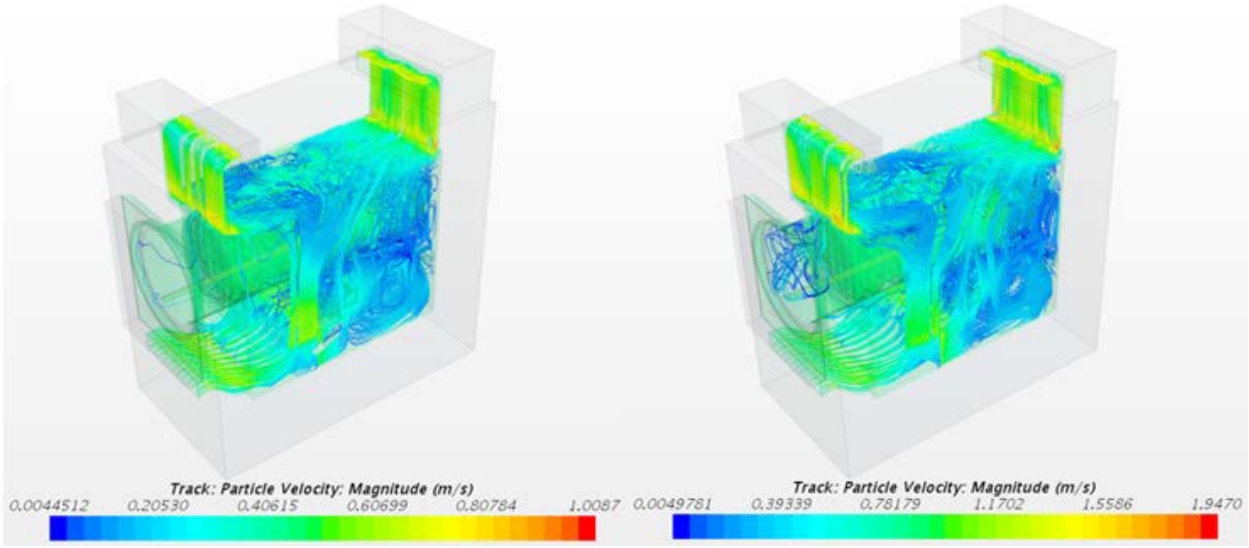

Figure 47: Particle velocity for NUHOMS® Calvert Cliffs HSM-15: 5 kW heat load shown on the left and 35 kW heat load shown on the right.

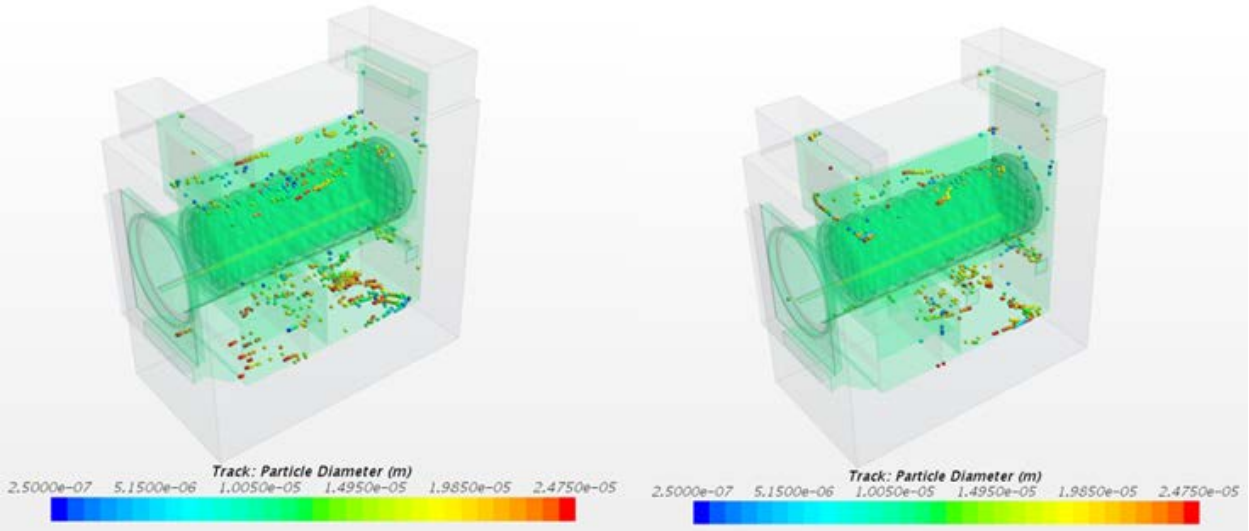

Figure 48: Overall particle deposition for NUHOMS® Calvert Cliffs HSM-15: 5 kW heat load shown on the left and 35 kW heat load shown on the right.

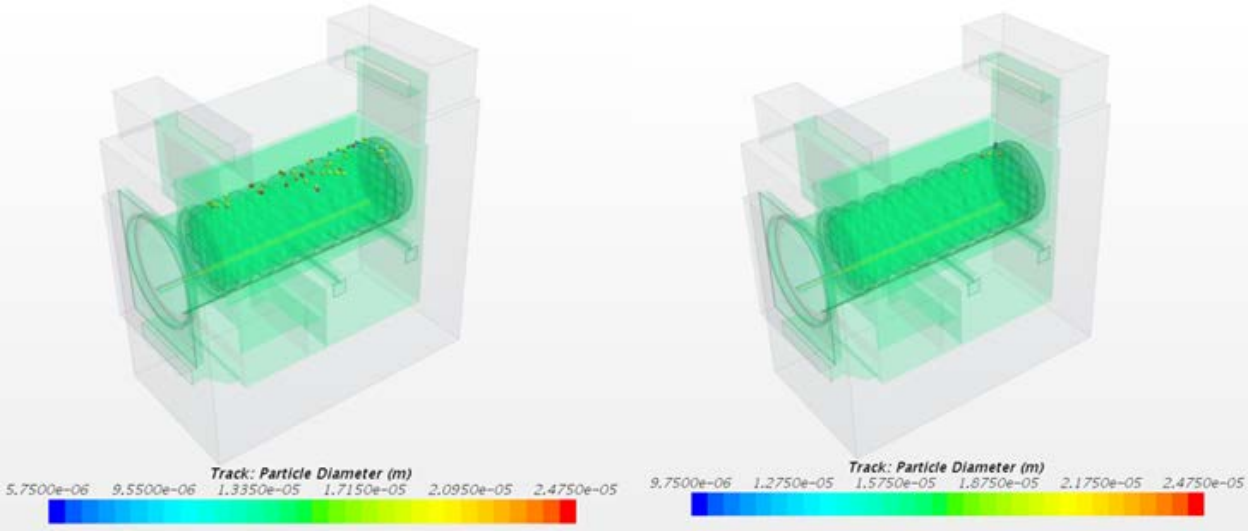

Figure 49: Canister particle deposition for NUHOMS® Calvert Cliffs HSM-15: 5 kW heat load shown on the left and 35 kW heat load shown on the right.

Detailed results showing the deposition results for individual components of the NUHOMS® system are shown in Table 2. Figure 50 shows the naming convention used for each component of the NUHOMS® system. Table 2 shows that the majority of the particles that enter the system exit the system without depositing on any surface. Of the particles that do deposit, the majority deposit on the concrete over pack. The key results for the DSC is that very little deposits on the canister and that the deposition on the canister increases with decreasing temperature.

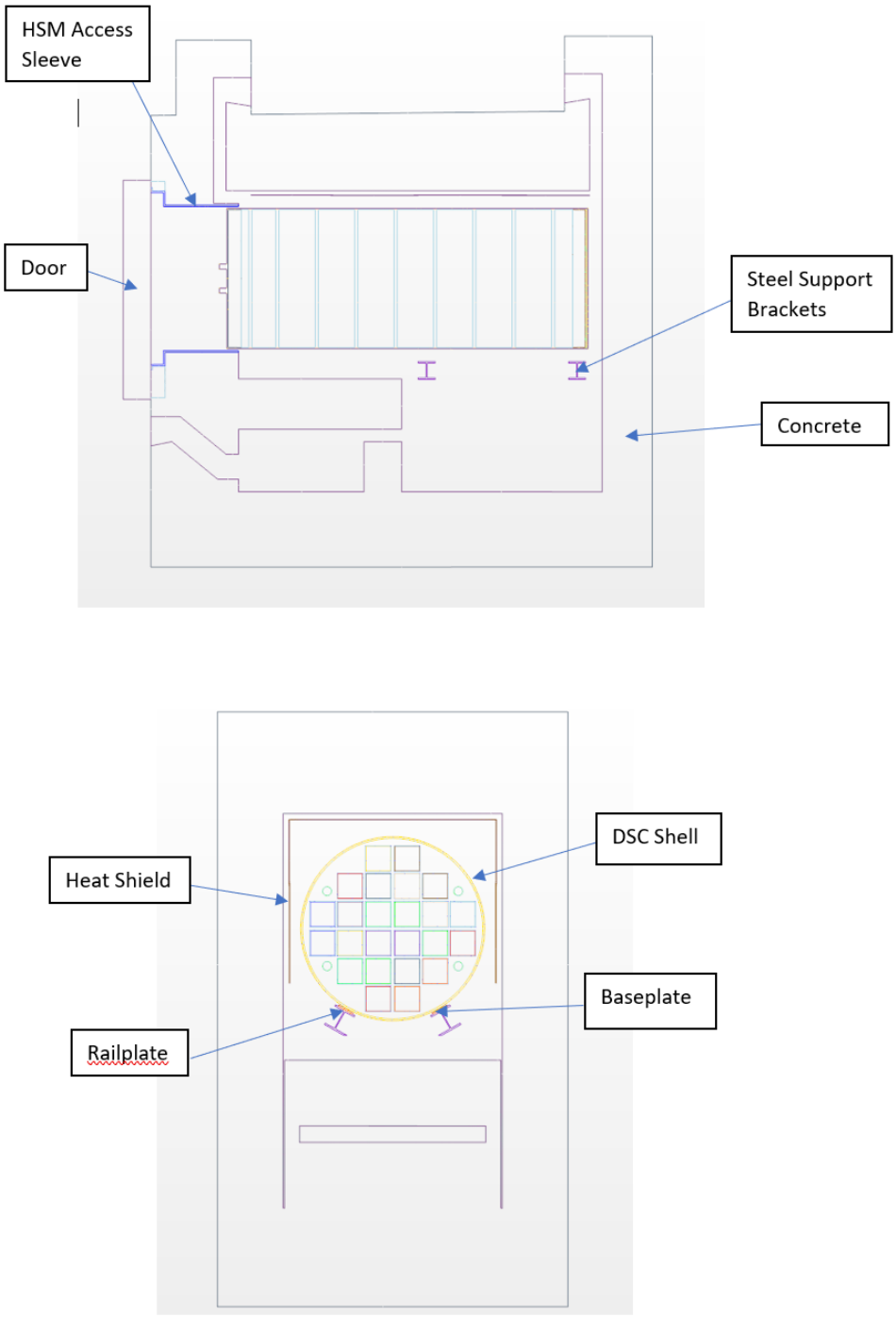

Figure 50: NUHOMS® component naming convention.

Table 2: NUHOMS® detailed deposition results.

Boundary	Heat Load [kW]	Particle Thermal Conductivity [W/m-K]	Avg Canister Surface Temp [C]	Max Canister Surface Temp [C]	Avg Inlet Velocity [m/s]	Avg Air Velocity [m/s]	Inlet Mass Flowrate [kg/s]	Stuck Mass Flowrate [kg/s]	DSC Deposition Efficiency	Deposition Efficiency
Baseplate (carbon steel)	5	0.613	50.96	95.27	0.44	0.17	2.00E-10	0.00E+00		0.00%
Concrete (concrete)	5	0.613	50.96	95.27	0.44	0.17	2.00E-10	6.64E-11		33.21%
Door (concretel)	5	0.613	50.96	95.27	0.44	0.17	2.00E-10	0.00E+00		0.00%
DSC Shell (stainless steel)	5	0.613	50.96	95.27	0.44	0.17	2.00E-10	6.42E-12	3.21%	3.21%
Heat Shield (stainless steel)	5	0.613	50.96	95.27	0.44	0.17	2.00E-10	1.32E-11		6.58%
HSM Access Sleeve (carbon steel)	5	0.613	50.96	95.27	0.44	0.17	2.00E-10	0.00E+00		0.00%
Railplate (carbon steel)	5	0.613	50.96	95.27	0.44	0.17	2.00E-10	0.00E+00		0.00%
Steel Support Brackets (carbon steel)	5	0.613	50.96	95.27	0.44	0.17	2.00E-10	7.47E-12		3.74%
Total Air Boundaries	5	0.613	50.96	95.27	0.44	0.17	2.00E-10	9.35E-11		46.74%
Baseplate (carbon steel)	10	0.613	71.65	147.23	0.53	0.21	2.00E-10	0.00E+00		0.00%
Concrete (concrete)	10	0.613	71.65	147.23	0.53	0.21	2.00E-10	6.08E-11		30.42%
Door (concretel)	10	0.613	71.65	147.23	0.53	0.21	2.00E-10	0.00E+00		0.00%
DSC Shell (stainless steel)	10	0.613	71.65	147.23	0.53	0.21	2.00E-10	4.11E-12	2.05%	2.05%
Heat Shield (stainless steel)	10	0.613	71.65	147.23	0.53	0.21	2.00E-10	1.32E-11		6.58%
HSM Access Sleeve (carbon steel)	10	0.613	71.65	147.23	0.53	0.21	2.00E-10	0.00E+00		0.00%
Railplate (carbon steel)	10	0.613	71.65	147.23	0.53	0.21	2.00E-10	0.00E+00		0.00%
Steel Support Brackets (carbon steel)	10	0.613	71.65	147.23	0.53	0.21	2.00E-10	1.06E-11		5.32%
Total Air Boundaries	10	0.613	71.65	147.231	0.53	0.21	2.00E-10	8.87E-11		44.37%
Baseplate (carbon steel)	15	0.613	89.68	190.54	0.60	0.24	2.00E-10	0.00E+00		0.00%
Concrete (concrete)	15	0.613	89.68	190.54	0.60	0.24	2.00E-10	5.85E-11		29.26%
Door (concretel)	15	0.613	89.68	190.54	0.60	0.24	2.00E-10	0.00E+00		0.00%
DSC Shell (stainless steel)	15	0.613	89.68	190.54	0.60	0.24	2.00E-10	2.74E-12	1.37%	1.37%
Heat Shield (stainless steel)	15	0.613	89.68	190.54	0.60	0.24	2.00E-10	1.07E-11		5.37%
HSM Access Sleeve (carbon steel)	15	0.613	89.68	190.54	0.60	0.24	2.00E-10	0.00E+00		0.00%
Railplate (carbon steel)	15	0.613	89.68	190.54	0.60	0.24	2.00E-10	0.00E+00		0.00%
Steel Support Brackets (carbon steel)	15	0.613	89.68	190.54	0.60	0.24	2.00E-10	9.68E-12		4.84%
Total Air Boundaries	15	0.613	89.68	190.535	0.60	0.24	2.00E-10	8.17E-11		40.84%
Baseplate (carbon steel)	20	0.613	106.08	227.87	0.66	0.26	2.00E-10	0.00E+00		0.00%
Concrete (concrete)	20	0.613	106.08	227.87	0.66	0.26	2.00E-10	5.69E-11		28.47%
Door (concretel)	20	0.613	106.08	227.87	0.66	0.26	2.00E-10	0.00E+00		0.00%
DSC Shell (stainless steel)	20	0.613	106.08	227.87	0.66	0.26	2.00E-10	2.11E-12	1.05%	1.05%
Heat Shield (stainless steel)	20	0.613	106.08	227.87	0.66	0.26	2.00E-10	8.95E-12		4.47%
HSM Access Sleeve (carbon steel)	20	0.613	106.08	227.87	0.66	0.26	2.00E-10	0.00E+00		0.00%
Railplate (carbon steel)	20	0.613	106.08	227.87	0.66	0.26	2.00E-10	0.00E+00		0.00%
Steel Support Brackets (carbon steel)	20	0.613	106.08	227.87	0.66	0.26	2.00E-10	1.07E-11		5.37%
Total Air Boundaries	20	0.613	106.08	227.874	0.66	0.26	2.00E-10	7.87E-11		39.37%
Baseplate (carbon steel)	25	0.613	121.58	258.95	0.70	0.28	2.00E-10	2.11E-13		0.11%
Concrete (concrete)	25	0.613	121.58	258.95	0.70	0.28	2.00E-10	5.72E-11		28.58%
Door (concretel)	25	0.613	121.58	258.95	0.70	0.28	2.00E-10	1.05E-13		0.05%
DSC Shell (stainless steel)	25	0.613	121.58	258.95	0.70	0.28	2.00E-10	1.47E-12	0.74%	0.74%
Heat Shield (stainless steel)	25	0.613	121.58	258.95	0.70	0.28	2.00E-10	9.58E-12		4.79%
HSM Access Sleeve (carbon steel)	25	0.613	121.58	258.95	0.70	0.28	2.00E-10	0.00E+00		0.00%
Railplate (carbon steel)	25	0.613	121.58	258.95	0.70	0.28	2.00E-10	0.00E+00		0.00%
Steel Support Brackets (carbon steel)	25	0.613	121.58	258.95	0.70	0.28	2.00E-10	1.12E-11		5.58%
Total Air Boundaries	25	0.613	121.58	258.951	0.70	0.28	2.00E-10	7.97E-11		39.84%
Baseplate (carbon steel)	30	0.613	135.95	281.46	0.74	0.30	2.00E-10	1.05E-13		0.05%
Concrete (concrete)	30	0.613	135.95	281.46	0.74	0.30	2.00E-10	5.29E-11		26.47%
Door (concretel)	30	0.613	135.95	281.46	0.74	0.30	2.00E-10	1.05E-13		0.05%
DSC Shell (stainless steel)	30	0.613	135.95	281.46	0.74	0.30	2.00E-10	1.47E-12	0.74%	0.74%
Heat Shield (stainless steel)	30	0.613	135.95	281.46	0.74	0.30	2.00E-10	9.26E-12		4.63%
HSM Access Sleeve (carbon steel)	30	0.613	135.95	281.46	0.74	0.30	2.00E-10	0.00E+00		0.00%
Railplate (carbon steel)	30	0.613	135.95	281.46	0.74	0.30	2.00E-10	0.00E+00		0.00%
Steel Support Brackets (carbon steel)	30	0.613	135.95	281.46	0.74	0.30	2.00E-10	1.01E-11		5.05%
Total Air Boundaries	30	0.613	135.95	281.464	0.74	0.30	2.00E-10	7.40E-11		37.00%
Baseplate (carbon steel)	35	0.613	149.59	305.99	0.78	0.32	2.00E-10	0.00E+00		0.00%
Concrete (concrete)	35	0.613	149.59	305.99	0.78	0.32	2.00E-10	5.55E-11		27.74%
Door (concretel)	35	0.613	149.59	305.99	0.78	0.32	2.00E-10	1.05E-13		0.05%
DSC Shell (stainless steel)	35	0.613	149.59	305.99	0.78	0.32	2.00E-10	8.42E-13	0.42%	0.42%
Heat Shield (stainless steel)	35	0.613	149.59	305.99	0.78	0.32	2.00E-10	9.37E-12		4.68%
HSM Access Sleeve (carbon steel)	35	0.613	149.59	305.99	0.78	0.32	2.00E-10	1.05E-13		0.05%
Railplate (carbon steel)	35	0.613	149.59	305.99	0.78	0.32	2.00E-10	0.00E+00		0.00%
Steel Support Brackets (carbon steel)	35	0.613	149.59	305.99	0.78	0.32	2.00E-10	9.26E-12		4.63%
Total Air Boundaries	35	0.613	149.59	305.995	0.78	0.32	2.00E-10	7.52E-11		37.58%

This page is intentionally left blank.

4. CONCLUSIONS AND FUTURE WORK

Deposition modeling was performed for two SNF canisters systems (MAGNASTOR® and NUHOMS®) and the SNL DCS. This modeling utilized the well-established PNNL thermal models and paired them with a particle tracking and deposition model. Deposition results were obtained for various decay heat rates, and at different locations in the canister system. The SNL DCS model also closely investigated the effects of particle size and developed a wind effects model to examine the effects of driving wind on particle deposition.

In all cases, the majority of the particles which entered the canister system exited without interacting with a surface. In addition, very little deposition was seen on the canister itself. For the two canister system models (MAGNASTOR® and NUHOMS®) very little (in some cases less than 1%) of what entered the system deposited on the canister walls, which is the region most susceptible CISCC. These results are shown in Table 1 and Table 2. However, it is important to note, that these results should not be taken at this time to imply that the total mass loading on the canisters is low. To determine the total mass loading on a canister, one would need to know the actual contaminant load in the air. Currently, there is very little information available concerning the atmospheric contaminant concentration at ISFSI sites. The lack of ISFSI contaminant information, also drove the decision to use a uniform particle size distribution as an input to these models. The uniform particle size distribution is hypothetical, and it is important to note that the deposition results are a function of this hypothetical input. In the future, when actual ISFSI site contaminant data is available, these models could be easily adapted to use these actual data sets. The models presented herein are a useful capability for analyzing canister performance and a good first step in understanding the deposition of corrosive contaminants on canister surfaces, but many information gaps remain.

Future work is needed to further refine these models, and to verify and validate the results. The model results presented herein are presented for information only.

Future model refinement is needed to incorporate additional functionality, such as a multi-phase model which allows for the effects of humidity to be included in the models. In addition, future modeling will incorporate additional deposition mechanism and perform additional analytical studies to assess the importance of each mechanism.

Future testing is needed to verify and validate the results obtained from the models. Verification and validation is necessary to extend the applicability of these models and to confirm the methodologies developed for this effort.

This page is intentionally left blank.

5. REFERENCES

Camuffo, Dario. “Dry Deposition of Airborne Particulate Matter: Mechanisms and Effects.” In Microclimate for Cultural Heritage, 283-346. Massachusetts: Elsevier, 2014.

Dassault Systemes SolidWorks Corp. 2017. SolidWorks Premium 2017 x64 Edition (computer software). Waltham, Massachusetts: Dassault Systemes.

Durbin, S.G. and E.R. Lindgren. 2017. Thermal-Hydraulic Results for the Boiling Water Reactor Dry Cask Simulator. SAND2017-10551: Sandia National Laboratories, Albuquerque, New Mexico.

Electric Power Research Institute, “Susceptibility Assessment Criteria for Chloride-Induced Stress Corrosion Cracking (CISCC) of Welded Stainless Steel Canisters for Dry Cask Storage Systems”. 2015, EPRI Report No 3002005371

Fort, J.A., Michener, T.E., Suffield, S.R., and Richmond, D.J. (2016). *Thermal Modeling of a Loaded MAGNASTOR Storage System at Catawba.* PNNL-25757: Pacific Northwest National Laboratories, Richland, Washington.

Greenfield, C. and Quarini, G. (1998). *A Lagrangian simulation of particle deposition in a turbulent boundary layer in the presence of thermophoresis.* Applied Mathematical Modeling 22, 759-771.

Gong S, Barrie L, and Blanchet J, “Modeling sea-salt aerosols in the atmosphere: 1. Model development,” Journal of Geophysical Research: Atmospheres, vol. 102, no. D3, pp. 3805–3818, Jan. 1997

Housiadas, C., Kissane, M., and Sehgal, R. “Fission Product Release and Transport” in Safety in Light Water Reactors, 425-517. Academic Press, 2012.

Jensen PJ, T Tran, BG Fritz, FC Rutz, SB Ross, AM Gorton, R Devanathan, P Plante, and K Trainor 2016. "Preliminary Evaluation of the DUSTRAN Modeling Suite for Modeling Atmospheric Chloride Transport." Air Quality Atmosphere and Health, May 2016, doi:10.1007/s11869-016-0404-5

Jordan, C. E., Pszenny, A. A., Keene, W. C., Cooper, O. R., Deegan, B., Maben, J., . . . Young, A. H. (2015). Origins of aerosol chlorine during winter over north central Colorado, USA. *Journal of Geophysical Research: Atmospheres,120*(2), 678-694. doi:10.1002/2014jd022294

Lau, T. and Nathan, G. “Influence of Stokes Number on the Velocity and Concentration Distributions in Particle-Laden Jets.” Journal of Fluid Mechanics 757 (2014): 432-457.

Lewis, E and Schwartz, S. *Sea salt aerosol production: mechanisms, methods, measurements and models- A critical review*. Washington: American geophysical union, 2004

Li, A. and Ahmadi, G. “Dispersion and Deposition of Spherical Particles from Point Sources in a Turbulent Channel Flow.” Aerosol Science and Technology 16 (1992): 209-226.

Milford, J. B., & Davidson, C. I. (1985). The Size of Particulate Trace Elements in the Atmosphere—A Review. *Journal of the Air Pollution Control Association,35*(12), 1249-1260. doi:10.1080/00022470.1985.10466027

Reeks, M. “The Transport of Discrete Particles in Inhomogeneous Turbulence.” Journal of Aerosol Science 14 (1983): 729-739.

Saffman, P. “The Lift on a Small Sphere in a Slow Shear Flow.” Journal of Fluid Mechanics 22 (1965): 385-400.

Sagot, B., Antonini, G., and Buron, F. (2009). *Annular flow configuration with high deposition efficiency for the experimental determination of thermophoretic diffusion coefficients.* Journal of Aerosol Science 40, 1030-1049.

Siemens. (2019). *STAR-CCM+ Users Guide, version 14.02*. Siemens Product Lifecycle Management Software, Inc.

Siemens PLM Software. 2019. STAR-CCM+ 14.02 (computer software). Plano, Texas: Siemens PLM Software.

Suffield, S.R., Richmond, D.J., and Fort, J.A. (2019). *Modeling of the Boiling Water Reactor Dry Cask Simulator*. PNNL-28424: Pacific Northwest National Laboratories, Richland, Washington.

Suffield, S.R., Fort, J.A., Adkins, H.E., Cuta, J.M., Collins, B.A., and Siciliano, E.R. (2012). *Thermal Modeling of NUHOMS HSM-15 and HSM-1 Storage Modules at Calvert Cliffs Nuclear Power Station ISFSI.* PNNL-21788: Pacific Northwest National Laboratories, Richland, Washington.

Sugiyama, G., Gowardhan, A., Simpson, M., Nasstrom, J. "Deposition Velocity Methods for DOE Site Safety Analyses." Lawrence Livermore National Laboratory, 2014. LLNL-TR-654366.

Taiwo, A. M., Beddows, D. C., Shi, Z., & Harrison, R. M. (2014). Mass and number size distributions of particulate matter components: Comparison of an industrial site and an urban background site. *Science of The Total Environment,475*, 29-38. doi:10.1016/j.scitotenv.2013.12.076

Talbot, L., Cheng, R., Schefer, R., and Willis, D. "Thermophoresis of Particles in a Heated Boundary Layer." Journal of Fluid Mechanics 101 (1980): 737-758.

Tang, Y. "Computational Fluid Dynamics Study of Aerosol Transport and Deposition Mechanisms." PhD diss., Texas A&M University, 2012.

Tang I, Tridico A, and Fung K, "Thermodynamic and optical properties of sea salt aerosols," *Journal of Geophysical Research: Atmospheres*, vol. 102, no. D19, pp. 23269–23275, Jan. 1997.

U.S. Nuclear Regulatory Commission, "Continued Storage of Spent Nuclear Fuel," 10CFR Part 51, Federal Register, 79, No. 182, Washington, DC (2014).

U.S. Nuclear Regulatory Commission, "Potential Chloride-Induced Stress Corrosion Cracking of Austenitic Stainless Steel and Maintenance of Dry Cask Storage System Canisters," Washington, DC (2012), ADAMS Accession No ML12319A440.

Xia, L., & Gao, Y. (2010). Chemical composition and size distributions of coastal aerosols observed on the US East Coast. *Marine Chemistry,119*(1-4), 77-90. doi:10.1016/j.marchem.2010.01.002

Young, J. and Leeming, A. "A Theory of Particle Deposition in Turbulent Pipe Flow." Journal of Fluid Mechanics 340 (1997): 129-159.

Zhao, Y. and Gao, Y. (2008). *Mass size distributions of water-soluble inorganic and organic ions in size-segregated aerosols over metropolitan Newark in the US east coast*. Atmospheric Environment 42, 4063-4078.